Chemical Engineering Journal 547 (2026) 180087

Contents lists available at ScienceDirect

Chemical Engineering Journal

journal homepage: www.elsevier.com/locate/cej

A two-step casting-coating strategy for multifunctional porous membranes enabling photothermal conversion, oil-water separation, and cationic dye separation

Zhuomin Jiang [a,1], Shuqing Piao [a,1], Daehong Kim [b,1], Yejin Lee [a], Chuang Zhu [c], Jihoon You [b], Dongwook Kang [b], Won Bo Lee [b,d,*], Yuanzhe Piao [a,e,*], Kangwon Lee [a,f,*]

[a] Department of Applied Bioengineering, Graduate School of Convergence Science and Technology, Seoul National University, Seoul, 08826, Republic of Korea
[b] Department of Chemical and Biological Engineering, Institute of Chemical Processes, Seoul National University, Seoul, 08826, Republic of Korea
[c] Shanghai Frontiers Science Center of Advanced Textiles, College of Textiles, Donghua University, Shanghai, 201620, China
[d] School of Transdisciplinary Innovations, Seoul National University, Seoul, 08826, Republic of Korea
[e] Advanced Institutes of Convergence Technology, Suwon-si, Gyeonggi-do, 16229, Republic of Korea
[f] Research Institute for Convergence Science, Seoul National University, Suwon-si, Gyeonggi-do, Republic of Korea

ARTICLE INFO

Keywords:
Dual pore-forming agents
Acid-hydrolyzed porous cellulose microspheres
Oil-water separation
Cationic dye rejection
Nonsolvent-induced phase separation

ABSTRACT

Nitrogen and organic-rich wastewater from industrial and agricultural activities poses a major threat to global water sustainability. In aquatic ecosystems, nitrogen accumulation drives eutrophication and threatens human health, necessitating efficient denitrification. Although conventional denitrification depends on external chemical additives (e.g., carbon sources), its temperature-dependent nature implies that localized thermal regulation can substantially lower chemical demand by accelerating reaction kinetics. To leverage this effect sustainably, embedding photothermal materials into filtration membranes for solar-driven localized heating offers an efficient approach for concurrent pollutant interception and chemical-saving remediation. Additionally, the negative charge of these materials enables simultaneous filtration of cationic pollutants. The substrate membrane was fabricated by a single-step phase inversion method using recycled poly(ethylene terephthalate) (rPET) together with polyvinylpyrrolidone (PVP) and hydrolyzed porous cellulose (hC) microspheres as pore-forming agents. A coating layer composed of negatively charged ZnO nanorods and Fe_3O_4@ACNT composites is applied on top of the membrane, which also increases the density of surface pores and provides multiple functionalities. Experimental results show that the membrane achieves oil/water separation efficiency of up to 99.5%. When exposed to simulated solar irradiation at 1500 W/m^2 the membrane heats itself to a temperature as high as 79.6 °C. Meanwhile, separation efficiencies exceed 95% for all tested cationic dyes. These results demonstrate that the developed porous composite membrane is a promising and eco-friendly choice for environmental remediation.

1. Introduction

Mitigating water pollution remains a critical global challenge, with municipal wastewater treatment plants (MWWTPs) facing increasingly stringent effluent total nitrogen (TN) limits [1]. Achieving efficient biological denitrification remains constrained by winter low-temperature inhibition (<15 °C) and high carbon-dosing operational costs, which typically exceed 50% of total wastewater treatment expenses [2,3]. Solar-driven photothermal materials offer an eco-friendly approach to introduce localized heating capable of fundamentally reactivating enzymatic pathways and accelerating denitrification kinetics at low temperatures [4,5]. However, their utilization is predominantly limited to solar evaporation and distillation systems instead of pressure-driven porous filtration membranes [6]. This application gap severely restricts the potential of photothermal platforms in treating complex industrial and agricultural source waters that concurrently contain emulsified oils and organic dyes [7,8]. To bridge this gap, integrating photothermal components directly into porous filtration matrices to verify their solar-to-thermal response and baseline multi-contaminant separation capabilities is an essential first step.

* Corresponding authors.
E-mail addresses: wblee@snu.ac.kr (W.B. Lee), parkat9@snu.ac.kr (Y. Piao), kangwonlee@snu.ac.kr (K. Lee).
[1] Zhuomin Jiang, Shuqing Piao, and Daehong Kim contributed equally to this work.

https://doi.org/10.1016/j.cej.2026.180087
Received 18 December 2025; Received in revised form 20 July 2026; Accepted 28 July 2026
Available online 31 July 2026
1385-8947/© 2026 Elsevier B.V. All rights are reserved, including those for text and data mining, AI training, and similar technologies.

High-performance membrane separation systems, including reverse osmosis (RO), nanofiltration (NF), ultrafiltration (UF), and microfiltration (MF), serve as the cornerstone of advanced water purification [9–11]. Among various fabrication techniques, nonsolvent-induced phase separation (NIPS) remains the most widely adopted and environmentally benign strategy, yielding porous matrices via rapid solvent/nonsolvent exchange between a cast polymer film and a water bath [12–14]. Generally, ongoing advancements in NIPS membranes focus on two parallel avenues: optimizing surface structures (e.g., porosity and specific surface area) and integrating high-performance composite components to augment functional capabilities [15–17]. Despite its viability, conventional NIPS still suffers from intrinsic structural control limitations, where high sensitivity to solution composition and water exchange kinetics often leads to non-uniform pore size distributions and interfacial instability [18,19]. Inspired by the highly porous architecture and exceptional adsorption properties of natural lava rock [20–22], this study incorporated hydrolyzed porous cellulose (hC) microparticles alongside polyvinylpyrrolidone (PVP) as dual pore-forming templates to resolve these structural limitations. Benefiting from the robust hydrophilicity and uniform morphology of both low-molecular-weight PVP and the lava rock-like hC microspheres, their uniform dispersion in the dope solution stabilizes the phase separation kinetics, thereby facilitating the single-step formation of a homogeneous porous membrane scaffold. Furthermore, the integration of these hydrophilic pore-forming agents significantly accelerates water permeation, thereby synergistically enhancing the baseline oil/water separation efficiency.

On the other hand, integrating multi-component nanomaterials within the NIPS membrane matrix is required to achieve functional capabilities beyond physical sieving. Specifically, transition-metal oxides (Fe_3O_4 and ZnO) and carbon nanotubes (CNTs) are utilized to enable both electrostatic adsorption of cationic contaminants and solar-to-thermal conversion via non-radiative electronic relaxation [4]. However, two critical engineering bottlenecks must be addressed when blending these materials into porous membranes: the structural leaching of Fe_3O_4 nanoparticles during dynamic filtration, and the severe flux decline often caused by nanomaterial aggregation. To prevent nanoparticle loss, Fe_3O_4 was grown in situ on acid-treated carbon nanotubes (ACNTs), where surface oxygen-containing groups stabilize the magnetic phase and utilize the conjugated π-system of CNTs to maximize light absorption [23–25]. Concurrently, one-dimensional (1D) ZnO nanorods were incorporated as a complementary photothermal agent; their 1D morphology provides additional thermal generation while creating low-resistance interfacial pathways to accelerate water transport. Bridging these material design strategies into a unified processing platform is essential for creating high-performance, self-heating membranes capable of treating complex wastewater.

Herein, we report a multi-functional porous composite membrane fabricated via a two-stage strategy to bridge plastic waste upcycling with advanced water purification Scheme 1. First, a sustainable porous membrane was prepared through a single-step nonsolvent-induced phase separation (NIPS) process, utilizing recycled poly(ethylene terephthalate) (rPET) as the polymer backbone, blended with polyvinylpyrrolidone (PVP) and lava rock-like hydrolyzed cellulose (hC) microspheres as dual pore-forming agents. Subsequently, the rPET scaffold underwent surface functionalization with Fe_3O_4@ACNT hybrids and ZnO nanorods to form a broadband photothermal coating, successfully integrating localized thermal generation, physical oil-water sieving, and electrostatic adsorption. Under solar irradiation, the photothermal coating induces a localized temperature elevation of 30–50 °C at the membrane interface. This localized heat generation is designed to overcome thermodynamic barriers and accelerate bacterial denitrification at low temperatures without external energy inputs, thereby potentially alleviating reliance on external carbon dosing. Simultaneously, leveraging its tailored wettability and surface negative charges, the composite membrane achieves concurrent high-flux oil-water separation and efficient cationic dye capture. Overall, this integrated material design provides a low-carbon, multi-functional paradigm for advanced effluent upgrading.

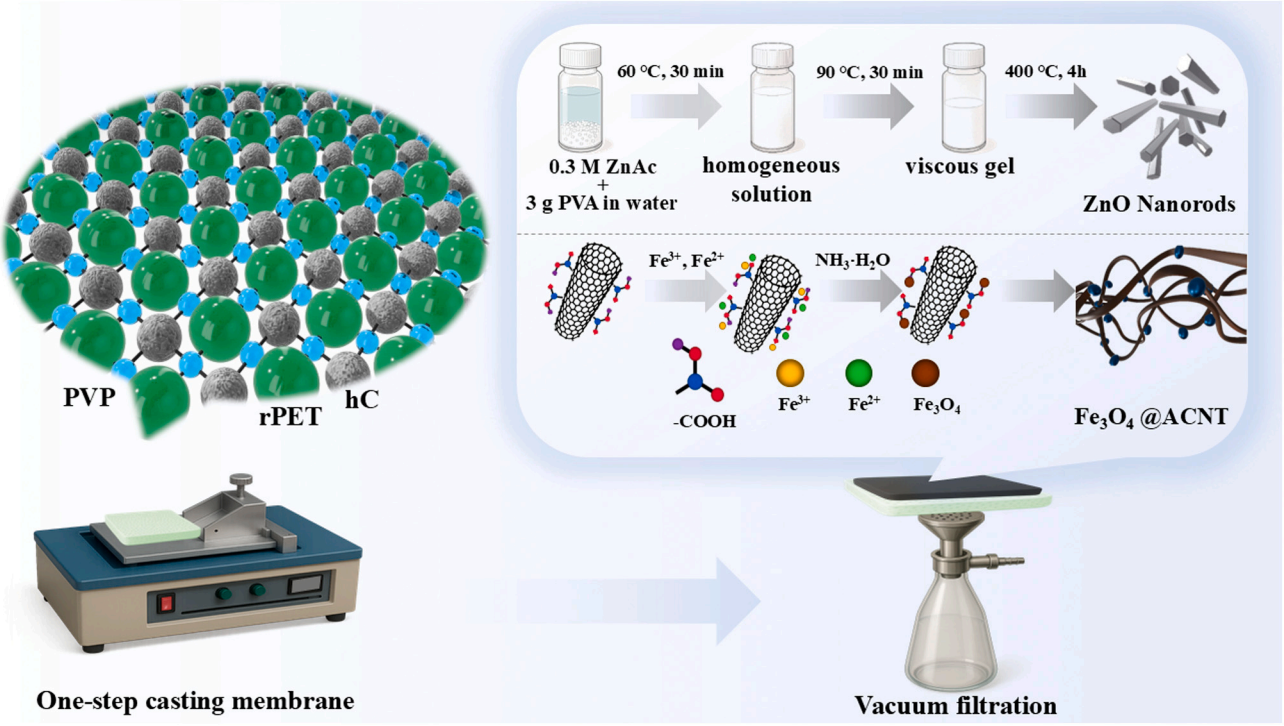

Scheme 1. The scheme of rPET/hC/PVP/ZnO nanorods/Fe_3O_4@ACNT membrane.

2. Experimental section

2.1. Materials

Polyethylene terephthalate (PET) bottles were collected from JIRISAN Mulhana (FINEBio, Korea). Trifluoroacetic acid (TFA) (99.0%) were purchased from DAEJUNG chemicals & Metals Co. Nitric acid (68.0–70.0%), Sulfuric acid (95.0%), n-Hexane (96.0%) and Mineral oil were acquired from Samchun pure chemical Co., LTD. Iron(III) chloride hexahydrate (97.0%), Polyvinylpyrrolidone (PVP) (Mw = 55,000, 40,000 and 10,000), polyvinyl alcohol (PVA), Carbon nanotube (multi-walled) (MWCNTs), Oil-red, Dopamine hydrochloride, Tween 40, Cellulose, Crystal violet, Toluidine blue, Rhodamine B, Methylene blue, Rose bengal, Indigo carmine, Methyl orange, Alizarin red S, Prussian blue and Zinc acetate dihydrate (99.0%) were acquired from Sigma Aldrich. Iron (II) chloride tetrahydrate was purchased from Kanto. 10 mM Tris-HCl (pH = 8.5) was purchased from Biosesang. Sodium dodecyl sulfate (SDS) was purchased from Junsei chemical Co.

2.2. Hydrolysis treatment of lava rock-like cellulose microspheres

Hydrolyzed cellulose (hC) microspheres with a lava rock-like structure were prepared by mixing 10 *g* of cellulose was added to 100 *mL* of 1 *M* sodium hydroxide solution and maintaining stirring for 4 h at room temperature. The pretreated cellulose powder was then rinsed with deionized water by centrifuging until the pH reached 7, followed by freeze-drying and ready for the following process. Subsequently, 1.2 *g* of the freeze-dried cellulose powder was hydrolyzed in 60 *mL* of 85% phosphoric acid at 50 °C for 36 h, during which the solution gradually turned into a yellowish transparent liquid. The hydrolyzed porous microspheres were precipitated by adding deionized water in ten times volume of the reaction mixture. The precipitated lava rock-like hC microspheres were then thoroughly rinsed using deionized water until neutral pH was obtained and then freeze-dried to obtain the final product.

2.3. Casting rPET/hC/PVP membrane

The recycled plastic bottles were thoroughly rinsed and cut into small pieces of $5 \times 5\ mm^2$. The PET pieces were sanitized twice with 70% ethanol and ultrasonicated for 30 min each time, followed by vacuum drying overnight and UV sterilization for 6 h. To prepare the rPET casting solution, 0.675 *g* PET, 0.225 *g* PVP, and 0.75 *g* hC microspheres were dissolved in 14 *g* TFA under magnetic stirring. Following complete dissolution achieved by magnetic stirring, the solution was cast onto a glass plate at a speed of 35 *mm/S* using a casting machine to form a membrane with a thickness of approximately 150 μm. The cast membrane was immediately quenched in ice water for phase separation and demolding, followed by vacuum-drying to obtain the final membrane.

2.4. Synthesis of acid carbon nanotubes (ACNTs)

0.5 *g* of MWCNTs was dispersed in a mixture of concentrated acid solution, which composed of sulfuric acid and nitric acid mixed in a 3:1 volume ratio. The resulting suspension was subjected to reflux at 70 °C for 4 h under constant stirring to ensure efficient oxidation and surface functionalization of the MWCNTs. After the reaction, the mixture was cooled to room temperature and rinsed several times with deionized water to remove residual acids and reaction byproducts, until the filtrate reached a neutral pH (pH = 7). The obtained ACNTs were then collected and dried for further use.

2.5. Synthesis of Fe_3O_4@ACNT nanoparticles

Fe_3O_4@ACNTs nanoparticles were synthesized via a one-step precipitation method. Firstly, 0.2 g of ACNTs were dispersed in 100 mL of distilled water. Then a 100 mL solution containing 0.5 g of $FeCl_2{\cdot}4H_2O$ and 1.0 g of $FeCl_3{\cdot}6H_2O$ was added to the ACNTs mixture and stirred for 30 min. Subsequently, $NH_3{\cdot}H_2O$ was added dropwise to adjust pH to 12, and the mixture was stirred at 50 °C for 1 h. Finally, the residues were collected and washed with water, ethanol and dried to obtain the final product.

2.6. Synthesis of zinc oxide (ZnO) nanorods (NRs)

For the preparation of ZnO nanorods, 0.3 M zinc acetate dihydrate and 0.3 g of PVA were dissolved in 100 mL of ethanol and magnetically stirred at 60 °C for 30 min to obtain a uniform precursor solution. The introduction of PVA promoted the directional growth of ZnO and served simultaneously as a capping and stabilizing agent. Subsequently, the temperature was raised to 90 °C and maintained for another 30 min to transform the solution into a gel-like phase. The resulting gel was dried and then calcined at 400 °C for 4 h to enhance the crystallinity of the ZnO nanorods.

2.7. Preparation of rPET/PVP/hC/ZnO NR/Fe_3O_4@ACNT composites

The rPET/PVP/hC/ZnO NR/Fe_3O_4@ACNT composite membranes were prepared by using a vacuum-assisted filtration process. Taking the rPET/PVP/hC/ZnO NR/Fe_3O_4@ACNT (1:2) composite as an example, 10 mg of ZnO NRs and 20 mg of Fe_3O_4@ACNT were dispersed in 10 mL of Tris-HCl buffer solution with 2 mg/mL of Dopamine hydrochloride (pH = 8.5). The dispersion was ultrasonicated to ensure homogeneity and then filtered through a preformed rPET/PVP/hC membrane. Following the filtration, the obtained membrane was subjected to vacuum drying at room temperature to remove residual moisture. Similarly, composite membranes with ZnO NR:Fe_3O_4@ACNT ratios of 1.5:1.5 and 2:1 were prepared by using the same steps, resulting in uniform and stable multifunctional rPET/PVP/hC/ZnO NR/Fe_3O_4@ACNT membranes that is ready for further characterization or application.

2.8. Characterizations

The surface morphology and elemental composition of the samples were examined using a field-emission scanning electron microscope (FE-SEM, JSM-7800F Prime, Japan). The structure and morphology of Fe_3O_4@ACNT was further investigated by transmission electron microscopy (TEM, JEM-3010, Japan). Organic materials were analyzed by attenuated total reflectance Fourier transform infrared spectroscopy (ATR-FTIR, TENSOR 27, Bruker, Germany). Inorganic materials were identified using X-ray diffraction (XRD, D8 Discover, Bruker, Germany). The photothermal performance of the membranes were tested by thermal imager (FLIR E5, USA) and thermometer (YET-610 L, UNI-T, China). Membrane thickness was measured by a digital micrometer (MDC-25PX, Mitutoyo, Japan). All tests were carried out at a temperature of 15 °C and 50% relative humidity under xenon lamp irradiation (WC-150, Wence, China). The light intensity was measured with a solar power meter (LX-107, Vici, China). The oil/water emulsion separation was compared under the optical microscope (Carl Zeiss Microscopy). The charge of materials was tested using a zeta potential analyzer (HORIBA, Japan). The thermal conductivity was measured with thermal conductivity meter (Thermtest MP-1, Thermtest Inc.). The absorption and reflectance spectra were -tested by the UV–vis-NIR spectrometer (Lambda 1050). The hydrophilicity of various membranes was evaluated using a water contact angle meter (KINO SL200KS) with a 10 μL water droplet applied each time. The ion concentration was determined by Inductively Coupled Plasma Optical Emission Spectrometer (ICP-OES, Agilent 5800).

2.9. Filtration measurements

The filtration performance of the membranes was systematically

assessed through demulsification tests, water permeation flux measurements, and separation efficiency evaluations using oil/water mixtures. Demulsification was performed by gravity-driven filtration using a glass funnel. Circular membrane samples were mounted on the funnel, and the effective filtration area (S) was calculated using the equation:

$$S = \pi r^2$$

The collected filtrates were subsequently examined under an optical microscope to evaluate phase separation behavior.

In contrast, water permeation flux and separation efficiency tests were evaluated using a vacuum-assisted filtration system operated at 1.5 bar. The demulsification performance of the rPET /PVP/hC/ZnO NR/Fe_3O_4@ACNT membrane was tested by the oil-in-water emulsions that stabilized with different types of surfactants. The mineral oil was pre-dyed by the Oil Red at the volume ratio of 30:1 to enhance visual contrast. For the ionic stabilizer system, 0.5 mL of dyed mineral oil was dispersed in 49.5 mL deionized water by 5 mg of SDS. In the nonionic stabilizer system, the solution was dispersed by 5 μL of Tween 40.

The water permeation flux of different coated membrane was tested by filtering 30 *mL* of deionized water under vacuum (1.5 bar), while recording the filtration time The flux was calculated using the following equation:

$$F = \frac{V}{P \bullet S \bullet t}$$

where F is the water flux ($L{\cdot}m^{-2}{\cdot}h^{-1}{\cdot}bar^{-1}$), V is the permeate volume in L, S is the effective contact area in m^2, P is the operating pressure in *bar*, t is the filtration time in *h*.

To assess oil/water emulsion separation efficiency, 0.5 mL of dyed mineral oil was mixed with 49.5 mL of deionized water and 5 μL of Tween 40 using a vortex mixer to form a stable emulsion. The filtrate was then extracted with hexane, and the residual oil concentration was determined from the absorbance at the characteristic dye peaks, calibrated against standard dyed oil.

To evaluate the anti-fouling ability of the composite membrane, the flux recovery rate (FRR) is defined as,

$$\mathrm{FRR} = \frac{J_{clean}}{J_{water}} \times 100\%$$

where J_{water} is the initial water flux, and J_{clean} is the water flux of the cleaned membranes after rising by ethanol and DI-water.

Further assessment of membrane fouling involves calculating the total fouling ratio (R_t), reversible fouling ratio (R_r), and irreversible fouling ratio (R_{ir}), these values are determined using the following equations:

$$R_t = \frac{J_{water} - J_{oil}}{J_{water}} \times 100\%$$

$$R_r = \frac{J_{clean} - J_{oil}}{J_{water}} \times 100\%$$

$$R_{ir} = \frac{J_{water} - J_{clean}}{J_{water}} \times 100\%$$

where J_{oil} is the flux of emulsion separation.

2.10. Dye rejection performance test of membranes

The dye rejection performance of the membranes was evaluated by gravity filtration. A dye solution with an initial concentration of 10 ppm was used as the control group. The feed dye solution (control) and filtrates of 1.5:1.5 and pristine samples were analyzed using UV–vis spectrophotometry. The dye rejection efficiency (R) of the membrane was calculated based on the absorbance values corresponding to the characteristic dye peaks using the following equation:

$$R(\%) = \left(1 - \frac{C_p}{C_f}\right) \times 100$$

where C_p and C_f represent the dye concentrations in the permeate and the feed solution (control), respectively.

3. Results and discussion

3.1. Morphological evolution and pore-forming mechanisms

The acid hydrolysis conditions play a decisive role in governing the macromolecular architecture of cellulose. As illustrated in Fig. 1a, severe acidic regimes (37% HCl) trigger an unguided, aggressive chemical cleavage of both amorphous and crystalline domains within the cellulose chains [26], while insufficient treatment with concentrated weak acids (short-term 85% H_3PO_4) results in non-uniform macromolecular swelling and chaotic structural collapse [27]. In either case, the cellulose matrix disintegrates into irregular fragments instead of ordered geometries. Conversely, a prolonged, mild hydrolysis in 85% H_3PO_4 for 36 h facilitates a controlled, top-down disintegration, yielding highly uniform hydrolyzed cellulose (hC) microspheres (2.21 ± 0.25 μm, Fig. S1a) [28]. This uniform spherical geometry, coupled with rich inherent hydroxyl groups, endows the hC microspheres with exceptional potential as sacrificial or structural pore-forming templates during membrane fabrication.

The distinct pore-forming behaviors between traditional polyvinylpyrrolidone (PVP) and the synthesized hC microspheres elucidate the underlying kinetics of the non-solvent induced phase separation (NIPS) process. Conventional water-soluble PVP chains often suffer from rapid, non-uniform leaching kinetics into the coagulation bath due to their linear macromolecular alignment, inevitably resulting in chaotic macrovoids with uncontrollable size distributions (Fig. S2) [29]. In sharp contrast, the stepwise incorporation of hC microspheres triggers a transition toward a highly interconnected, homogeneous porous network (Fig. 1b). From a mechanistic perspective, the highly hydrophilic hC microspheres act as localized water-affinity centers within the casting solution. Upon immersion in the non-solvent bath, these microspheres accelerate the local liquid-liquid demixing rate via enhanced thermodynamic instability, while their distinct spherical boundaries simultaneously serve as spatial barriers that suppress the unrestricted growth of catastrophic macrovoids [30]. Consequently, the 5% hC-tailored membrane optimizes the median pore diameter to 1.02 ± 0.03 μm and propels the overall porosity to an impressive 75% (Table S1). Compared with recently reported recycled poly(ethylene terephthalate) (rPET)-based membranes in literature [31,32], our hC-templated NIPS strategy successfully resolves the trade-off between high porosity and structural homogeneity, establishing a robust blueprint for upscaling rPET valorization.

3.2. Interfacial engineering of multi-dimensional coatings

Beyond internal pore regulation, the topographic architecture of the active layer was adjusted via the interfacial deposition of ZnO NRs and Fe_3O_4@ACNT hybrids. As evidenced by Fig. S3, the building blocks comprise zero-dimensional (0D) Fe_3O_4 nanoparticles (~7 nm) and one-dimensional (1D) ZnO NRs (~35 nm in diameter, ~232 nm in length). When assembled at varied mass ratios (Fig. 1c), the morphological density of the surface coating changes with the composition.

The tuning of the ZnO:Fe_3O_4@ACNT ratio to an optimized equilibrium (e.g., 1.5:1.5 or 1:2) forms a interconnected 0D-1D-1D multi-dimensional network. Within this architecture, the high-surface-area ACNTs function as a carbon scaffold that anchors and prevents the self-aggregation of the ultra-small Fe_3O_4 nanoparticles [33]. Simultaneously, the elongated ZnO NRs interweave across the ACNT bundles, filling the microscopic voids within the carbon matrix. This structural

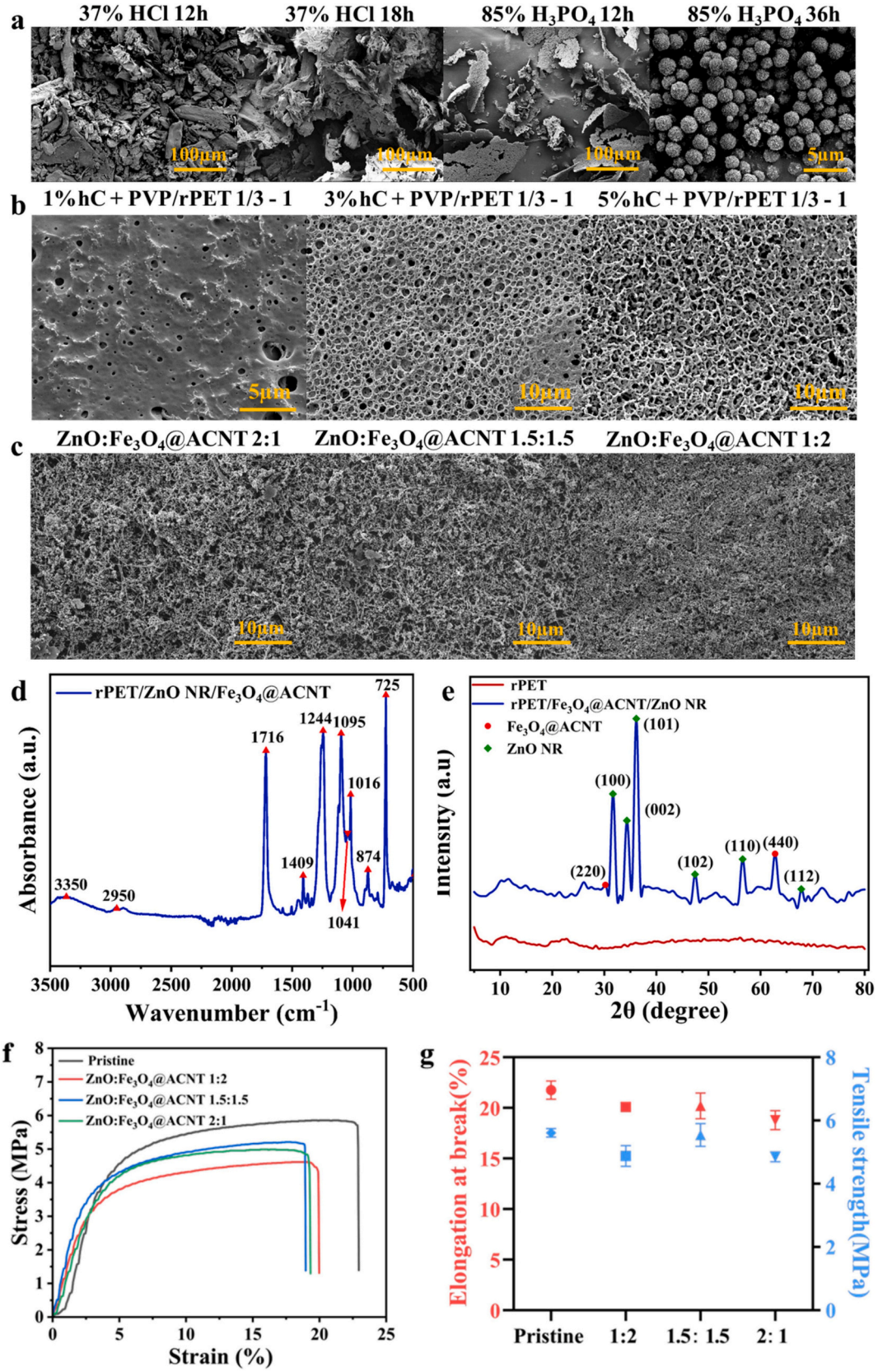

Fig. 1. (a) The SEM images of hydrolyzed cellulose (hC) in different conditions. (b) The surface structure of the casted membrane with different concentration of hC additive amount (1%, 3%, and 5%). (c) The surface structure with ZnO: Fe_3O_4@ACNT (1:2, 1.5:1.5, 2:1) vacuum-assisted coated on the rPET/hC/PVP membrane. The (d) ATR- FTIR and (e) XRD results for 1.5:1.5 ZnO:Fe_3O_4@ACNT-coated membrane. (f) Stress-strain curves of rPET/hC/PVP membrane and ZnO:Fe_3O_4@ACNT-coated membrane with ratios of 1:2, 1.5:1.5 and 2:1 and (g) corresponding tensile strength and elongation at break.

synergy increases the packing compactness and surface pore density of the top layer.

From an engineering perspective, this dense coating layer serves a dual purpose: it provides an interfacial barrier that mitigates membrane compaction under hydraulic pressure, while concurrently presenting an integrated platform optimized for subsequent photothermal conversion, size-exclusion dye rejection, and stable oil-water separation [34,35].

3.3. Macromolecular composition and crystal phase integrity

To clarify the chemical functionalities and phase structures of the composite membranes, Fourier-transform infrared (FTIR) and X-ray diffraction (XRD) analyses were carried out. As shown in Fig. 1d, the characteristic infrared bands of recycled poly(ethylene terephthalate) (rPET) are clearly resolved. Specifically, the sharp absorption band at 1716 cm^{-1} is ascribed to the ester C═O stretching vibration, while the prominent peaks at 1244 cm^{-1} and 1095 cm^{-1} correspond to the C-O-C and O-C-C asymmetric stretching vibrations in aromatic esters, respectively. Furthermore, the out-of-plane bending of para-substituted benzene rings at 874 cm^{-1} and the C—H bending at 725 cm^{-1} are well preserved [36,37]. This preservation of these primary ester and aromatic linkages indicates that the macromolecular backbone of rPET retained its chemical integrity throughout the recycling and phase-inversion protocols. This confirms the chemical stability of post-consumer rPET for use as a resilient membrane matrix.

Simultaneously, the successful incorporation of the synthesized hC microspheres and the PVP co-binder is confirmed. The broad, intense absorption band centered at 3350 cm^{-1} signifies the typical O—H stretching vibration of cellulose. Importantly, the broadening and slight shift of this hydroxyl band, combined with the attenuated intensity of the β-glycosidic linkage peak at 895 cm^{-1}, provide molecular-level evidence of the phosphoric acid-driven hydrolysis [38,39]. This trend indicates the partial cleavage of long-chain amorphous glucan networks and the disruption of the robust intermolecular hydrogen-bonding networks, which accounts for the highly porous and hydrophilic nature of the resulting hC microspheres. Together with the C—H stretching at 2950 cm^{-1} and pyranose ring C-O-C vibrations at 1041 cm^{-1} and 1016 cm^{-1}, the cellulose signature is verified. Moreover, the distinct peak at 1409 cm^{-1} originates from the CH_2 scissoring vibration within the PVP backbone, confirming the retention of the hydrophilic PVP macromolecular modifier within the integrated polymer matrix [40].

The crystalline phase purity and interfacial assembly of the inorganic functional coating layer were further interrogated via XRD (Fig. 1e). The distinct diffraction reflections emerging at $2\theta = 30.21^\circ$ and 62.8° are indexed to the (220) and (440) crystallographic planes of cubic inverse spinel magnetite, confirming the structural integrity of the Fe_3O_4 nanostructures anchored onto the ACNTs [41]. Concurrently, a series of sharp, well-defined diffraction peaks at $2\theta = 31.66^\circ$, 34.34°, 36.14°, 47.42°, 56.56°, and 67.86° are indexed to the (100), (002), (101), (102), (110), and (112) planes of hexagonal ZnO [42], respectively [43,44].

3.4. Mechanical robustness and interfacial stress transfer

The mechanical integrity of separation membranes is a critical prerequisite for enduring long-term hydraulic pressure and resisting physical deformation in practical water-treatment engineering. Accordingly, uniaxial tensile tests were performed to evaluate the tensile strength, Young's modulus, and elongation at break of the membranes (Fig. 1f and g). The pristine membrane delivered a tensile strength of 5.61 ± 0.14 MPa, a Young's modulus of 0.77 ± 0.03 MPa, and an elongation at break of 21.76 ± 0.91%. Following the surface modification and interfacial deposition of multi-dimensional ZnO/Fe_3O_4@ACNT hybrids, the tensile strength was maintained within a range of 4.85–5.54 MPa. These minor variations indicate that the subsequent interfacial coating protocol did not induce chemical degradation or macroscopic structural defects within the pristine membrane [45], thereby preserving the foundational load-bearing architecture required for sustainable filtration operations [46].

Importantly, the Young's modulus exhibited an increasing trend, reaching 0.92 ± 0.16 MPa, 0.98 ± 0.18 MPa, and 0.89 ± 0.31 MPa for the composite membranes with ZnO:Fe_3O_4@ACNT mass ratios of 1:2, 1.5:1.5, and 2:1, respectively. This structural stiffening effect is governed by the localized intercalation and interlocking of rigid inorganic nanofillers within the polymeric sub-layers [47]. The multi-dimensional combination of 0D Fe_3O_4 and 1D ZnO NRs creates a network of interlocking points that restrict the free relaxation of the surrounding polymer domains under external stress.

Concurrently, the elongation at break exhibited a marginal contraction to 20.10 ± 0.36%, 20.20 ± 1.27%, and 18.77 ± 0.95%. This reduction in macro-ductility is a characteristic feature of nanofiller-reinforced polymers, stemming from the restricted segmental mobility of the rPET and PVP chains [48]. The high surface energy of the nanohybrids exerts localized physical constraints, preventing the long-chain macromolecules from sliding past one another during tensile elongation.

From a practical engineering perspective, balancing mechanical stiffness with operational flexibility is essential. Despite the inorganic loading, the composite membranes maintain a stable Young's modulus coupled with a preserved elongation profile (~20%). This mechanical balance ensures that the membrane retains elasticity and bendability. Such mechanical durability is highly desirable for standard industrial modular packaging (e.g., spiral-wound or pleated configurations) and allows the membrane to withstand hydraulic fluctuations, continuous cross-flow shear, and periodic backwashing without encountering delamination or structural rupture [49].

3.5. Surface wetting dynamics and underwater oleophobicity

The surface wetting behavior of the composite membranes was characterized by water contact angle (WCA) and underwater oil contact angle (UWCA) measurements (Fig. 2a). The pristine rPET/hC/PVP substrate exhibited a hydrophilic nature with a WCA of 14.63 ± 0.79°. This behavior is driven by the integration of the hydrophilic hC microspheres (Fig. S5) and PVP pore-formers, which enhance the surface energy and water-adsorption capacity of the rPET matrix [50]. Upon the interfacial deposition of the ZnO/Fe_3O_4@ACNT composite, the WCA increased to 22.72° - 44.85°. This trend is attributed to the partial shielding of the hydrophilic polymer functional groups by the inorganic composite coating, coupled with the introduction of a hierarchical surface topography. Despite this change, all coated membranes maintained a WCA below 50°, confirming the retention of their surface-hydrophilic property.

Importantly, the evolution in underwater oil-repellency highlights the influence of the multi-dimensional coating. While the pristine membrane displayed a moderate UWCA of 116.1°, the functionalized counterparts achieved a transition into the underwater superoleophobic regime, with UWCAs exceeding 150° (e.g., 154.17° for the 1:2 ratio).

This wetting transition can be interpreted through the lens of the Cassie-Baxter state adapted for underwater environments. The hierarchical roughness provided by the 1D ZnO NRs and the Fe_3O_4@ACNT scaffold facilitates the entrapment of a stable, thin hydration layer within the inter-particle voids. According to the Cassie-Baxter model, this trapped water layer acts as a physical barrier that minimizes the effective contact area between the oil droplets and the solid surface, thereby imposing an effective underwater oleophobic repulsion against oil fouling [51]. The ZnO:Fe_3O_4@ACNT (1.5:1.5) configuration was selected as the optimized interface due to its balanced combination of high hierarchical roughness and persistent surface hydrophilicity.

The structural robustness of this underwater superoleophobic interface was further evidenced by the detachment of dichloromethane (DCM) droplets during compression testing (Fig. 2c). This low-adhesion behavior is essential for practical oil/water separation. This

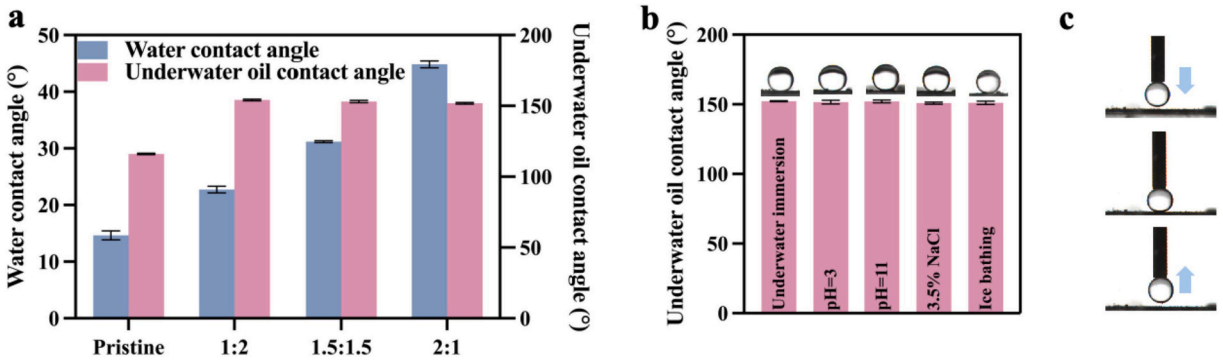

Fig. 2. (a) Water contact angles (WCA) and underwater oil contact angles (UWCA) of different membranes; (b) UWCA of the ZnO:Fe_3O_4@ACNT-coated membrane with a ZnO:Fe_3O_4@ACNT ratio of 1.5:1.5 after different treatments; (c) Underwater oil-repellent behavior of the ZnO:Fe_3O_4@ACNT-coated membrane (ZnO:Fe_3O_4@ACNT = 1.5:1.5).

characteristic suppresses the oil-fouling propensity that serves as a common failure mode in industrial filtration, ensuring that captured oil droplets can be readily swept away by the permeate stream [52]. Consequently, the synergy between the high-energy hydration layer driven by the rPET/hC/PVP substrate and the micro-nanoscale hierarchical roughness imposed by the ZnO/Fe_3O_4@ACNT coating creates an integrated anti-fouling architecture, providing a sustainable solution for high-throughput oil-water purification.

3.6. Emulsion permeation behavior and mass transport resistance

The structural suitability and surface adaptability of the engineered composite membranes were evaluated using both anionic (SDS) and non-ionic (Tween40) surfactant-stabilized oil-in-water emulsions. These two benchmark systems pose distinct interfacial behaviors, where the SDS-stabilized droplets feature electrostatic repulsion, whereas the Tween40-stabilized matrices are governed by steric hindrance. Investigating both configurations provides a comprehensive assessment of the wettability-mediated separation capacity of the membrane [53].

As shown by the optical microscopy profiling (Fig. 3a), all modified membranes achieved high purification efficacy for both emulsion types, with no detectable residual oil droplets in the collected filtrates. This microstructural separation correlates with the clear transparency of the treated effluents (Fig. 3b). Dynamic light scattering (DLS) analysis revealed a mean droplet size of 4.48 ± 3.53 μm for the SDS emulsion (Fig. 3c) and 8.42 ± 7.11 μ*m* for the Tween40 emulsion (Fig. 3d). The successful interception of these sub-10 μm and sub-micron emulsified matrices highlight the separation efficiency of the membrane pore network [54].

To investigate the fluid dynamics, the cross-sectional thicknesses of the active and support layers were quantified (Fig. 3e). All membranes maintained an ultra-thin profile below 100 μm, which is favorable for minimizing internal mass transport resistance. However, a progressive loading of ZnO NRs expanded the total membrane thickness from 68.2 μm (pristine) to 91.2 μm (2:1 mass ratio), triggering a corresponding reduction in pure water permeance (Fig. 3f). The pristine membrane delivered a peak flux of 3926.52 ± 186.49 L m^{-2} h^{-1} bar^{-1}, whereas the 2:1 counterpart decelerated to2290.17 ± 65.50 L m^{-2} h^{-1} bar^{-1}.

According to Darcy's law, the accumulation of ZnO NRs increases the tortuosity of the surface pore channels and narrows the effective surface porosity, thereby increasing the intrinsic hydraulic resistance [55]. Nevertheless, when tested across varied transmembrane pressures (0.2–1.5 *bar*, Fig. S6), the permeation flux exhibited a linear correlation (R^2 > 0.99), confirming structural stability and high resistance to compaction under realistic pressure-driven operations.

This trade-off between permeance and selectivity was accompanied by high separation efficiencies (Fig. 3g). The 1.5:1.5 ZnO:Fe_3O_4@ACNT configuration sustained a stable separation efficiency of 99.34 ± 0.02%. When benchmarked against literature values (Table S3), our 1.5:1.5 membrane demonstrated competitive separation metrics while utilizing a simpler, more scalable casting methodology. The deployment of post-consumer rPET as the core structural skeleton further introduces clear life-cycle assessment (LCA) and sustainability advantages, reinforcing its potential for large-scale environmental engineering [56].

3.7. Interfacial anti-fouling mechanisms and robustness

To evaluate the durability of the optimized 1.5:1.5 composite membrane in aggressive operational environments, emulsion separation was performed under exposure to strong acids, alkalis, concentrated brines, and cryogenic conditions (12 h ice bath). As compiled in Fig. 3h, the separation efficiencies remained stable above 99.25% under all extreme conditions. The mechanical robustness of the hetero-coating was validated by a high-shear vortex agitation test (20 min, Fig. S7), which caused no observable delamination or nanoparticle detachment, confirming strong interfacial binding forces between the substrate and the multi-dimensional overlayer.

The interfacial anti-fouling mechanism was further probed via multi-cycle fouling analysis (Fig. 3i). When subjected to severe mineral oil emulsion fouling, the pristine rPET membrane suffered a rapid decline in performance, yielding a flux recovery rate (*FRR*) of only 77.6% due to direct oil adhesive fouling. Conversely, the ZnO:Fe_3O_4@ACNT engineered membranes demonstrated a substantial anti-fouling enhancement, elevating the *FRR* values above 88%.

A detailed analysis of the fouling resistance distribution reveals the underlying physical chemistry mechanism: Although all samples exhibited high total fouling ratios (R_t > 77%), the coated membranes experienced a substantial reduction in the irreversible fouling ratio (R_i ~ 11%) alongside a dominant increase in the reversible fouling ratio (R_r > 65%). From the perspective of surface chemistry and coordination energetics, the oxygen-containing and hydrophilic groups populated on the Fe_3O_4@ACNT significantly lower the interfacial tension against water, driving the spontaneous formation of a dense, tenacious hydration layer. This hydration shield prevents the oil droplets from establishing direct hydrophobic contact or strong van der Waals interaction with the underlying polymer matrix [57]. As a result, the oil fouling is restricted to a physically reversible state (R_r), which can be easily detached via simple hydraulic washing, thereby ensuring stable, long-term filtration cycles [58].

The practical separation versatility of the 1.5:1.5 membrane was demonstrated across a wide viscosity spectrum encompassing n-hexane, petroleum ether, silicone oil, and heavy mineral oil, maintaining separation efficiencies above 98.56% and *FRR* values above 81.8% (Fig. 3j). This broad applicability was successfully extended to industrial simulations using stable, multi-component wastewater containing chili oil and commercial detergents (Fig. S8). The system produced a clear

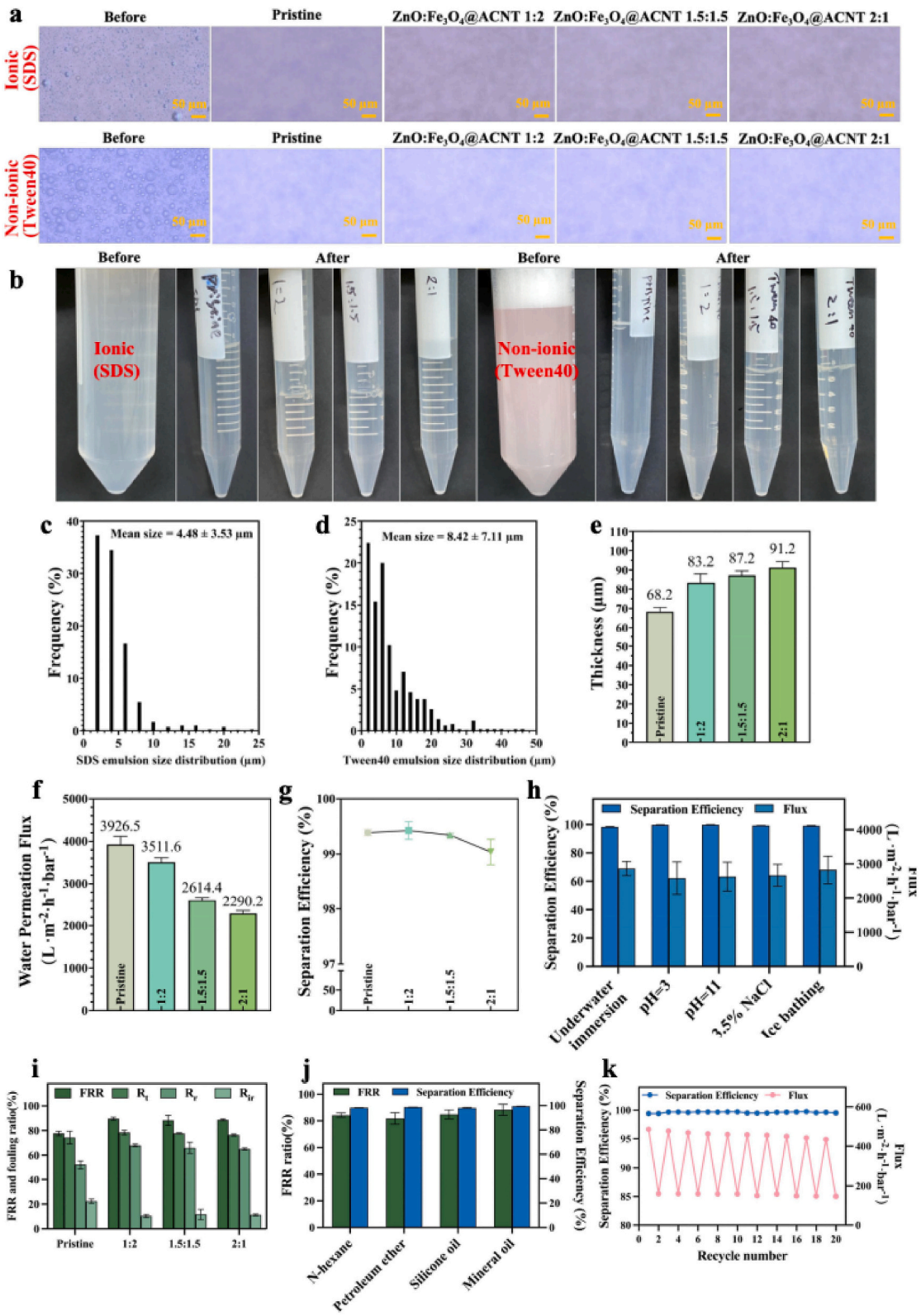

Fig. 3. (a) The optical microscopy results and (b) the photographs of oil-in-water emulsions stabilized by ionic (SDS) and non-ionic (Tween40) surfactants before and after separation by pristine, ZnO:Fe_3O_4@ACNT-coated membrane with ratios of 1:2, 1.5:1.5, and 2:1. The size distribution of the (c) ionic (SDS) emulsion and (d) non-ionic (Tween40) emulsion droplet before filtration. (e) Thickness analysis of pristine and coated membranes. (f) Water permeation flux and (g) Separation efficiency for various samples. (h) Water permeation flux and separation efficiency of the ZnO:Fe_3O_4@ACNT-coated membrane with ratios of 1.5:1.5 after being treated by different treatments. (i) The FRR, R_t, R_{ir}, and R_r of the pristine, ZnO:Fe_3O_4@ACNT-coated membrane with ratios of 1:2, 1.5:1.5, and 2:1, respectively. (j) The FRR and separation efficiency of the ZnO:Fe_3O_4@ACNT-coated membrane with ratios of 1.5:1.5 for various emulsions. (k) Emulsion permeance flux and separation efficiency of ZnO:Fe_3O_4@ACNT-coated membrane with ratios of 1.5:1.5 during 20 cycles.

filtrate with no volatile organic compounds or oil residues detected by optical verification, illustrating the capacity of the membrane to resist surfactant displacement and maintain structural integrity [59].

Finally, long-term operational durability and environmental safety were investigated (Fig. 3k). To address the potential risk of secondary environmental pollution caused by nanoparticle leaching, which represents a key constraint for practical engineering applications, ICP-OES profiling was conducted over extended cycling (Table S2). The analysis revealed that Fe remained nearly undetectable, while Zn leaching stabilized below a trace concentration of 0.2 mg L^{-1} even after 20 continuous vacuum-filtration cycles. This value sits safely below the strict World Health Organization (WHO) safety guidelines for drinking water, verifying the chemical stability and high environmental safety of the developed composite membrane for advanced water treatment [60].

3.8. Broadband photonic capture and band-gap layer engineering

The solar-to-thermal conversion efficiency of the functionalized membranes is predicated on their optical absorption capacity across the solar spectrum. Fig. 4a delineates the UV–Vis-NIR absorbance profiling of the integrated rPET/hC/PVP membranes tailored with varying ZnO NR:Fe_3O_4@ACNT mass ratios within the 250–2500 *nm* spectrum. The optimized hetero-engineered interface displays an efficient omnidirectional broadband light trapping effect, sustaining an average absorbance as high as ~97% across the entire interrogated spectral range.

A localized optical signature is registered near 370 nm, where a characteristic absorption edge emerges. This phenomenon is selectively governed by the intrinsic band-to-band electronic transitions of the hexagonal wurtzite ZnO NRs [61]. Correspondingly, the 2:1 configuration exhibits the highest excitonic peak intensity in this ultraviolet window, which progressively scales down as the ZnO weight fraction decreases in the 1.5:1.5 and 1:2 architectures.

Conversely, within the expansive visible and near-infrared (NIR) wavelengths (370–2000 *nm*), the absorbance curves exhibit a steady, gradual attenuation. This behavior is strongly modulated by the spatial density of the black Fe_3O_4@ACNT light-trapping matrix [62]. At the compositional ratio of 1.5:1.5, the structural synergy among the 1D ZnO NRs, 0D Fe_3O_4 nanoparticles, and the ACNT bundles reaches an optimal spatial configuration, establishing a highly efficient pathway for cross-interface charge transfer and broad-spectrum photon harvesting.

From the perspective of solid-state electronics, the heavily dispersed Fe_3O_4 nanostructures introduce dense mid-gap states within the energy band-gap [63], allowing for sub-bandgap photon excitation. Concurrently, the overlapping ACNT networks supply a highly conductive, continuous π-π conjugated electron sea that effectively delocalizes the photo-excited carriers and shifts the plasma resonance absorption deep into the low-energy NIR domain [64]. While an excess of Fe_3O_4@ACNT (1:2) leads to severe optical shadowing and detrimental backward Mie scattering, and redundant ZnO (2:1) limits long-wavelength photon extraction due to its wide band-gap (~3.2 *e*V), the 1.5:1.5 ternary hybrid achieves a robust balance, transforming the top layer into a near-ideal black-body absorber.

3.9. Lab-scale photothermal kinetics and energy localization

To translate this optical harvest into macroscale thermal energy, the photothermal kinetics of the functionalized rPET membrane platforms (2 × 2 cm^2) with varying compositional ratios were monitored under calibrated xenon lamp simulated solar irradiances (300–1500 W m^{-2}). As plotted in Fig. 4b, the steady-state saturation temperatures of the modified membranes exhibit a strong linear dependence against the square of the incident solar power density. This correlation confirms that the localized thermal dissipation of the interface can be precisely modulated by tuning the external radiation flux [65]. Among the candidates, the 1.5:1.5 hybrid yields the highest coefficient of determination (R^2 = 0.9952), signifying a highly efficient energy transformation network.

This kinetic performance is further verified by the real-time, time-dependent temperature profiles (Fig. 3c). Under a continuous illumination of 1500 *W* m^{-2}, the 1.5:1.5 membrane drives a rapid thermal response, leaping to a maximum localized surface temperature of 79.53 °C, far outperforming the other ratios. Consequently, this optimized composition was selected as the candidate for real-time solar-thermal water processing. As the simulation irradiance escalates from 300 to 1500 W m^{-2} (Fig. 4d), the peak surface temperature smoothly scales from 38.0 °C to 79.53 °C, demonstrating a consistent intensity-dependent output.

Periodic cyclic illumination sequences (Fig. 4f) reveal a stable and reproducible on-off photothermal profile, where the peak temperature consistently returning to ~78 °C over extended cycles with no noticeable thermal decay. This fast thermal responsive behavior is visually mapped by the real-time infrared thermography series (Fig. 4g). A rapid brightness transition occurs within merely 5–50 *s*, which highlights the membrane's capability for dynamic thermal management and instantaneous localized heating at the fluid interface [65].

3.10. Real-world outdoor adaptability and phase-change de-icing performance

To bridge lab-scale simulations with actual field operations, outdoor real-time temperature tracking was conducted on September 4, 2024, under variable meteorological conditions (Fig. S9). The membrane was exposed to realistic environmental conditions, including ambient temperatures of 20–31 °C, a relative humidity of ~68%, and wind shearing corresponding to Beaufort scale levels 1 to 4 (Fig. 4h).Upon data collection starting at 9:30 a.m., the membrane surface temperature rapidly ascended from 55.9 °C to a high of 73.6 °C by 11:30 a.m., moving in tandem with the increasing solar zenith angle and solar irradiance. Notably, during the afternoon hours when transient cloud layers intermittently obstructed the direct solar beams, the membrane temperature exhibited sensitive, instantaneous fluctuations but successfully stabilized around a high baseline of ~70 °C. This rapid temperature recovery upon re-illumination highlights the high optical sensitivity and minor thermal inertia of the active coating layer, demonstrating its technical applicability in unpredictable outdoor environmental engineering.

To quantitatively evaluate the solar-thermal phase-change capacity of the system, a comprehensive 3D profile correlating ice-thawing flux, incident solar intensity, and membrane surface temperature was constructed under halogen lamp exposure (Fig. 4i). Crucially, the 1.5:1.5 composite membrane exhibits a low intrinsic thermal conductivity of 0.443 W m^{-1} K^{-1} (Fig. S10). From a heat-transfer engineering perspective, this low thermal conductivity acts as a critical thermal barrier that suppresses downward conductive heat loss into the bulk polymer substrate, effectively confining the converted photothermal energy strictly at the top active interface [66]. Consequently, the ice-thawing volumetric flux of the 1.5:1.5 membrane expanded proportionally with light intensity and surface temperature, reaching peak thawing rate of 31.93 $L{\cdot}m^{-2}{\cdot}h^{-1}{\cdot}bar^{-1}$ under 1500 W m^{-2} illumination at 79.53 °C. In contrast, the pristine rPET counterpart exhibited a stable baseline rate of only 17.5 $L\ m^{-2}{\cdot}h^{-1}{\cdot}bar^{-1}$. The Fe_3O_4@ACNT scaffold serves as the broadband energy collector that drives the localized temperature lift, while the interweaving ZnO NRs act as localized thermal-conduction bridges that deliver this accumulated heat across the ice-membrane phase boundary [67]. This coordinated optimization of photonic collection and spatial heat localization establishes a green paradigm for solar-driven de-icing and advanced thermal-assisted environmental remediation.

3.11. Dye separation and interfacial mechanisms

The dye separation efficiency of the pristine and ZnO/Fe_3O_4@ACNT (1.5:1.5) coated membranes was evaluated using nine representative organic dyes with variant charges and molecular sizes (Fig. 5b). To

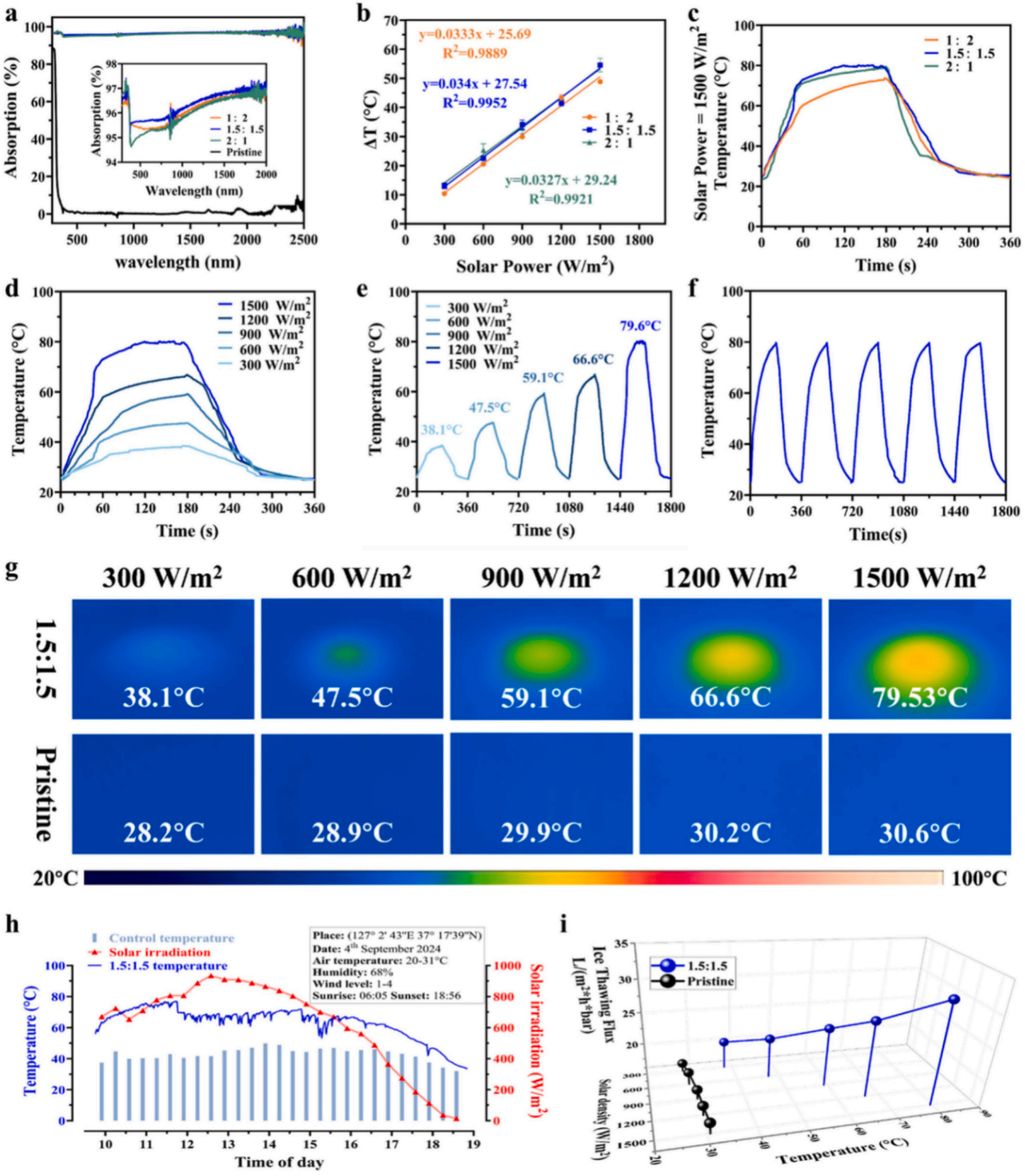

Fig. 4. Photothermal performance of coated rPET membrane under a xenon lamp illumination and investigation on photothermal mechanism. (a) UV–vis-NIR absorption spectra of the membranes. The inset shows the detailed data for the coated membranes in the 250 *nm* to 2000 *nm* wavelength range. (b) Linear relationship between ΔT and the different power densities. (c) Temperature variations of the membranes with a power density of 1500 W/m^2. (d)Temperature variations of membranes with different power densities. (e) Temperature variations of membranes at varied power densities of heating and cooling processes. (f) Five heating and cooling cyclic tests of membranes with a power density of 1500 W/m^2. (g) IR images of membranes corresponding to different power densities. (h) The recorded real-time temperature of the 1.5:1.5 membrane and ambient environment under natural light. (i) 3D relationship of Ice Thawing Flux, Solar Density, and Temperature for membrane.

prevent concentration-dependent dye aggregation, all feeding solutions were prepared at a standardized low concentration of 10 ppm (physicochemical properties are summarized in Table S4).

To investigate the surface charge properties, zeta potential measurements were conducted (Fig. 5a). The PVP/hC mixture (3:10), pristine ZnO NRs, and Fe_3O_4@ACNT all exhibited negative surface potentials. Upon the incorporation of the 1.5:1.5 ZnO:Fe_3O_4@ACNT composite, the surface negative charge was maintained at −18 mV. This negative surface charge provides a platform for investigating the competitive effects of size exclusion and electrostatic interactions [68,69].

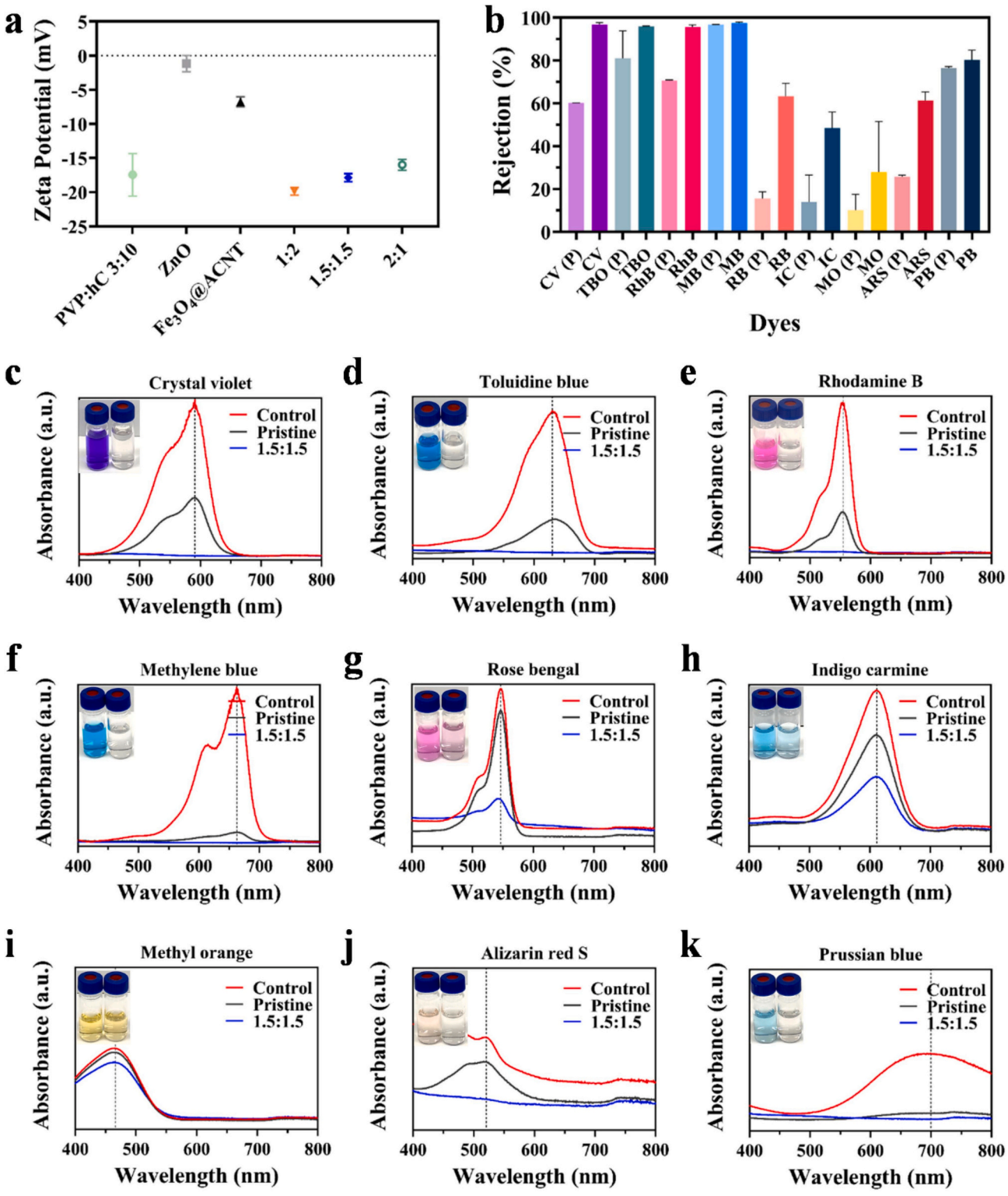

Fig. 5. (a) Zeta potential values of individual components (PVP:hC, ZnO, Fe_3O_4@ACNT) and composite ZnO:Fe_3O_4@ACNT dispersions with varying mass ratios (1:2, 1.5:1.5, 2:1), confirming surface charge characteristics. (b) Rejection efficiencies of various cationic and anionic dyes. UV–vis absorption spectra of feed (Control), filtrates from pristine rPET/hC/PVP membrane, and coated rPET/hC/PVP membrane (1.5:1.5) after filtration of each dye solution: (c) Crystal violet, (d) Toluidine blue, (e) Rhodamine B, (f) Methylene blue, (g) Rose bengal, (h) Indigo carmine, (i) Methyl orange, (j) Alizarin red S, (k) Prussian blue.

For the anionic dyes, including Rose Bengal (RB), Indigo Carmine (IC), Methyl Orange (MO), and Alizarin Red S (ARS), the pristine membrane (P) showed relatively low rejection efficiency (< 20%). At the 10 ppm dilution, these specific dyes exhibit high water solubility (~5–100 g L^{-1}) and exist as monodisperse hydrated ions with small molecular dimensions (1.2–2.0 nm), which allows them to pass through the larger pores of the pristine membrane. However, after coating with the 1.5:1.5 composite, the rejection rates significantly increased to 60% - 80%. This improvement is primarily attributed to the Donnan exclusion effect [70]. The enhanced negative charge density on the composite coating surface repels the co-ions of the anionic dye molecules, thereby increasing the resistance to their trans-membrane permeation.

In contrast, the composite membrane exhibited high removal efficiency (exceeding 95%) for all cationic dyes (CV, TB, RhB, and MB). The pristine membrane itself showed a high baseline rejection (60% - 95%), which is driven by the electrostatic adsorption of the positively charged dye molecules onto the electronegative surface of the rPET/hC/PVP matrix. Following top-layer modification with the 1.5:1.5 hybrid, the rejection rates were further enhanced to over 95%. This enhancement is ascribed to the interwoven network of 1D ZnO NRs and ACNTs, which reduces the effective pore size and intercepts dye molecules through physical sieving.

A distinct behavior was observed for Prussian Blue (PB). Despite being an anionic species, PB showed a stable rejection rate of approximately 80% on both the pristine and coated membranes, demonstrating low sensitivity to surface charge modifications. This phenomenon is rooted in its inorganic coordination chemistry.Because PB has an extremely low solubility product constant ($K_{sp} \approx 10^{-41}$) and is insoluble in water [71]. Consequently, even at a 10 *ppm* concentration, PB forms stable nanoscale colloidal aggregates in the aqueous phase. Because the dimensions of these colloidal clusters are larger than those of monodisperse dyes, its separation mechanism is dominated by size exclusion, where the large aggregates are physically blocked at the pore entry due to spatial steric hindrance.

The effective dye separation is further confirmed by the UV–Vis-NIR spectra and visual comparisons (Fig. 5c–k). The characteristic absorption peaks of the nine dyes decreased substantially after filtration, and the treated effluents transitioned into clear filtrates, particularly for the cationic species (Fig. 5c–f). In summary, the synergistic combination of size exclusion and electrostatic effects enabled the composite membrane to achieve selective and efficient removal of organic pollutants.

3.12. Theoretical study on interfacial mechanisms

3.12.1. Interfacial stability and fragment anchoring at the atomic level

To uncover the atomic-level interactions governing the structural integrity of the multi-component membrane, density functional theory (DFT) calculations were performed to evaluate the thermodynamic

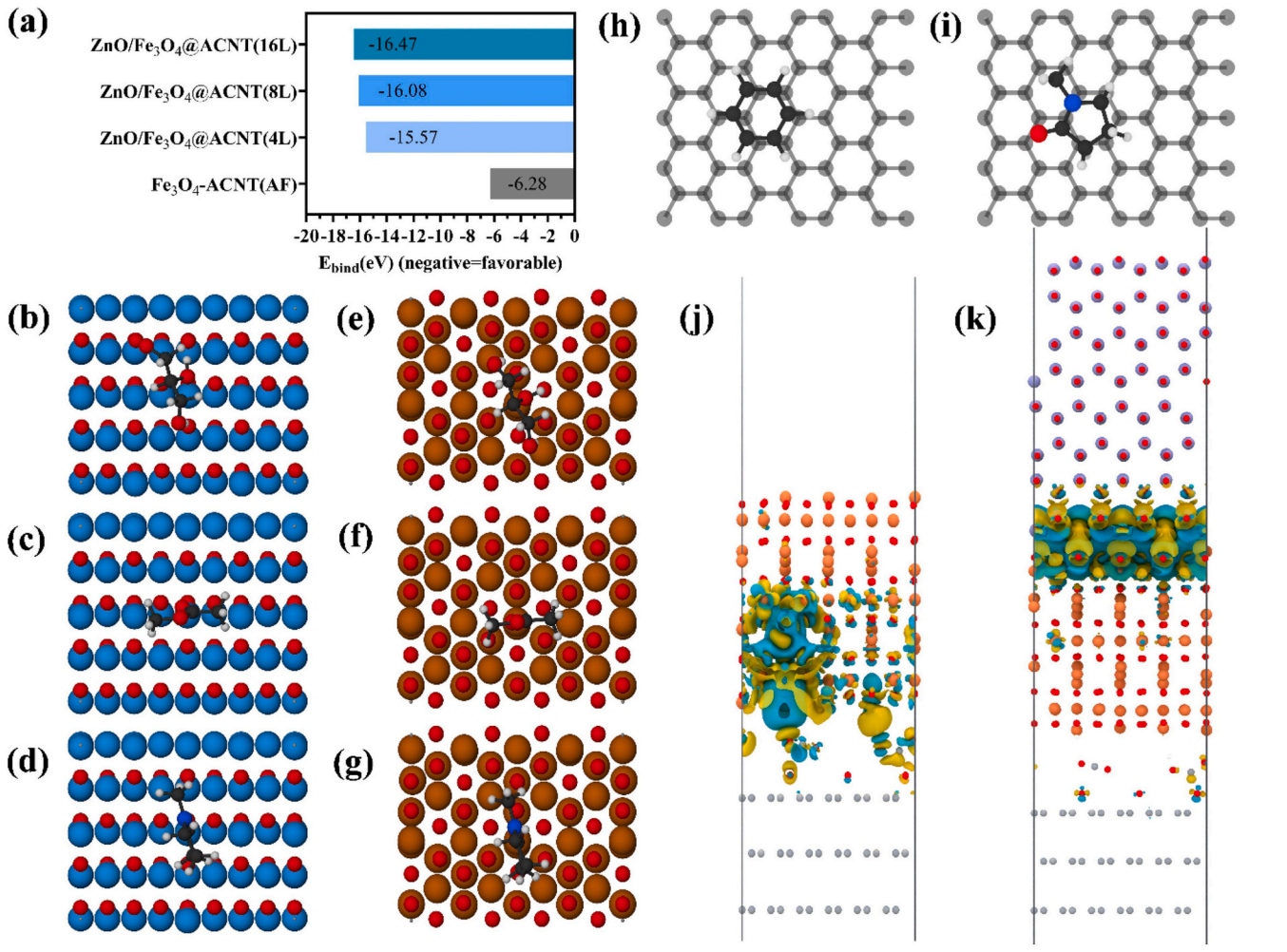

Fig. 6. Interfacial thermodynamics, electronic structures, and optimized polymer-fragment adsorption configurations. (a) Comparison of same-cell and area-normalized binding energies. Top views of optimized adsorption structures on constituent substrates: (b) GLY, (c) MA, and (d) NMP on ZnO; (e) GLY, (f) MA, and (g) NMP on Fe_3O_4; (h) BZ and (i) NMP on ACNT. Side-view charge density difference (CDD) isosurfaces (± 0.005 e $Å^{-3}$, yellow: accumulation, cyan: depletion) for (j) Fe_3O_4-ACNT and (k) 16-layer composite heterojunctions.

adhesion between the constituents (Fig. 6a). Such binding/formation-energy-based stability analyses are widely used in first-principles studies of layered and interfacial systems to evaluate heterostructure stability [72,73]. In Table 1, the calculated same-cell binding energy (E_{bind}) for the Fe_3O_4-ACNT interface is −6.28 *e*V, which corresponds to an area-normalized value of −0.81 J m^{-2}, supporting energetically favorable heterojunction formation in the constructed interface model. Upon the structural integration of ZnO onto the Fe_3O_4@ACNT substrate, the systems yield negative E_{bind} values of −15.57, −16.08, and −16.47 *e*V for the 4-, 8-, and 16-layer ZnO models, respectively (corresponding to area-normalized values of −2.01, −2.08, and −2.13 J m^{-2}). This thermodynamic favorability quantitatively substantiates that the assembled oxide-carbon architecture possesses structural stability against interfacial delamination during operation, consistent with the experimentally observed coating stability.

This macro-scale integrity is locally underpinned by atomic-level chemical restructuring at the heterogeneous interfaces. In the optimized Fe_3O_4@ACNT model, the oxygenated functionalities at the ACNT edge actively participate in surface anchoring through two distinct local motifs: one interfacial carboxyl group transfers its proton to a surface oxygen atom, establishing a short $d_{H-Osurf}$ bond of 0.98 Å, while an adjacent carboxyl group forms a close H—Fe contact of 2.08 Å.

This localized anchoring mechanism explains the high binding affinity between the oxide surfaces and the polymeric matrix embedded within the membrane. Oxygen-containing fragments within the polymer network, including glycerol (hydroxyl proxy for hC), methyl acetate (representing rPET), and *N*-methyl-2-pyrrolidone (representing PVP), exhibit preferential chemisorption on the Lewis-acidic sites of the oxide surfaces. In Table 2 and Fig. 6b-i, the calculated binding energies on ZnO are −3.994 eV for glycerol, −2.714 eV for methyl acetate, and −2.968 eV for *N*-methyl-2-pyrrolidone. In contrast, the graphitic carbon basal plane displays weaker, dispersion-dominated interactions with these polymer segments, as evidenced by the lower binding energies on pure ACNT (−1.6 to −1.74 eV). These distinct binding energy regimes provide a quantitative molecular explanation for why the integration of Fe_3O_4 and ZnO components successfully prevents polymer leaching and maintains the structural cohesion of the membrane [74–78].

3.12.2. Electronic structure and interfacial charge transfer dynamics

To establish the quantitative link between structural optimization and functional performance, charge-density-difference (CDD) and Bader charge analyses were employed to evaluate the electronic structure and charge transfer dynamics at the junctions. As shown in Fig. 6j-k, Fig. S14–16 and Table S6, a substantial electronic rearrangement occurs upon contact, characterized by a local charge redistribution of 0.5 *e* at the Fe_3O_4-ACNT interface and 0.62–0.65 *e* across the full ZnO/(Fe_3O_4@ACNT) heterojunctions.

Bader charge analysis of the 16-layer composite quantifies this electronic redistribution at the electronic level, revealing a net charge accumulation of −0.2 *e* on ACNT, and net charge depletions of +0.04 *e* on Fe_3O_4 and +0.15 *e* on ZnO. This polarization demonstrates that the composite oxides serve as collective electron donors, while the continuous ACNT network functions as a localized electron acceptor. This electronic redistribution vector is consistent with the work-function offset aligned across the vacuum level (Fig. 7a, b), a descriptor commonly interpreted together with CDD and Bader charge analysis in interfacial DFT studies [79]. The pristine components exhibit distinct work functions (4.65 *e*V for ACNT, 4.5 *e*V for Fe_3O_4, and 6 *e*V for clean ZnO), which equilibrate to yield an assembled work function of 5.57 *e*V for the composite heterojunction, creating an internal potential gradient that regulates carrier transport [80–83].

Table 2
Calculated binding energies of representative polymer fragments on the constituent surfaces.

Surface	Fragment	Interaction motif	Energy (eV)
ZnO	GLY	Hydroxyl-rich proxy for hC	−3.994
ZnO	MA	Ester/carbonyl proxy for rPET	−2.714
ZnO	NMP	Pyrrolidone carbonyl proxy for PVP	−2.968
Fe_3O_4	GLY	Hydroxyl-rich proxy for hC	−2.399
Fe_3O_4	MA	Ester/carbonyl proxy for rPET	−2.576
Fe_3O_4	NMP	Pyrrolidone carbonyl proxy for PVP	−2.676
ACNT	BZ	Aromatic proxy for rPET	−1.740
ACNT	NMP	Pyrrolidone carbonyl proxy for PVP	−1.600

This electronic polarization directly dictates the distinct roles played by each component during light harvesting and heat generation. First-principles DOS/PDOS and band-structure analyses are commonly used to interpret near-Fermi states and band alignment. Density of states (DOS) and projected DOS (PDOS) evaluations (Fig. 7c, d and Fig. S12-S13, S17-S20 and Table S7) show that wide-bandgap ZnO contributes negligibly near the Fermi level (E_F), meaning it remains photochemically inert in the low-energy spectrum [84–87]. Instead, the electronic states near E_F are heavily dominated by Fe *3d* (56%), C *2p* (23%), and O states (20%). In Fig. 7e-f, Table 3 and Fig. S21, BoltzTraP2 transport coefficients substantiate this distribution, where ACNT exhibits the dominant in-plane electronic conductivity descriptor ($\sigma/\tau = 7.7 \times 10^{17}\ S\,m^{-1}\,s^{-1}$) while ZnO acts as an insulator at E_F. Consequently, the electronic structure calculations demonstrate a clear cooperative mechanism: the continuous ACNT/Fe_3O_4 network establishes the primary conductive pathway for photothermal carrier relaxation, whereas ZnO functions exclusively as a surface-exposed functional regulator, including wetting and dye anchoring, rather than the near-Fermi conductive pathway [84,85,88–96].

3.12.3. Microscopic dye adsorption and composition optimization

The surface regulation provided by the oxide components was further examined through explicit atomic-level adsorption simulations of cationic dyes, using charge-compensated neutral MB + Cl^- and CV + Cl^- schemes to reduce net-charged periodic-cell artifacts (Fig. 8a, b) [97–103]. The calculated adsorption energies are strictly exothermic across all optimized configurations. For Methylene Blue (MB) and Crystal Violet (CV), the adsorption energies range from −2.54 to −0.82 eV and −3.07 to −0.85 eV in vacuum, respectively, and remain consistent upon the application of dipole corrections. In all variants (Fig. 8a-d and Table 4), the flat-lying "zzz" orientation emerges as the thermodynamically preferred geometry. This high stability stems from multidentate surface contacts: MB can expose terminal N sites together with central N/S-containing motifs, whereas CV is stabilized mainly through multiple terminal N-containing contacts and aromatic surface interactions.

To isolate the specific anchoring centers (Table 5 and Fig. 8e, f), local fragment calculations reveal that the sulfur motif (dimethyl sulfide) and the tertiary-amine motif (*N*,*N*-dimethylaniline) bind preferentially to ZnO over Fe_3O_4 by an energetic margin of 0.43–0.45 *e*V. This energetic

Table 1
Interfacial binding energies and Bader charge distributions for the composites.

System	E_{bind} (eV)	E_{bind}/A (eV $Å^{-2}$)	E_{bind}/A (J m^{-2})	ACNT (e)	Fe_3O_4 (e)	ZnO (e)
Fe_3O_4-ACNT	−6.28	−0.0506	−0.81	−0.029	+0.029	–
ZnO/Fe_3O_4@ACNT, 4 L	−15.57	−0.1255	−2.01	−0.144	−0.302	+0.446
ZnO/Fe_3O_4@ACNT, 8 L	−16.08	−0.1296	−2.08	−0.156	+0.194	−0.038
ZnO/Fe_3O_4@ACNT, 16 L	−16.47	−0.1327	−2.13	−0.197	+0.044	+0.154

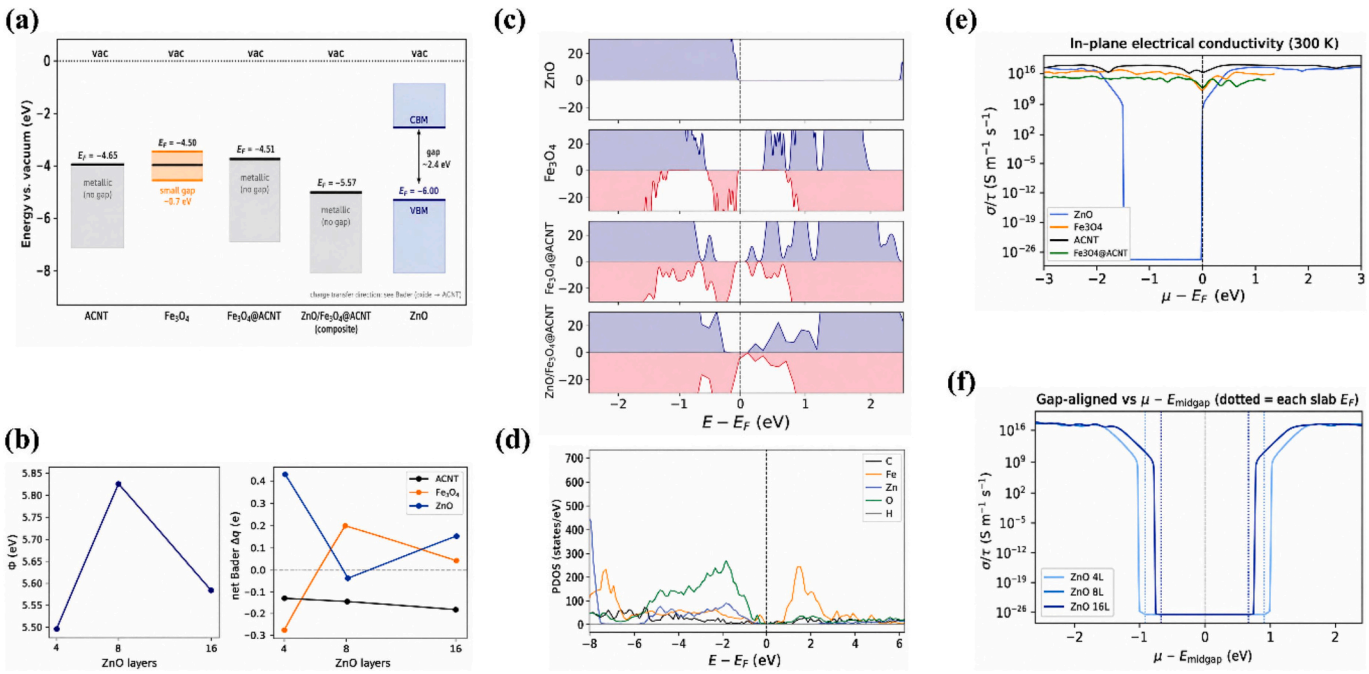

Fig. 7. Electronic structures, energy level alignments, and BoltzTraP2 electronic conductivity analysis. (a) Vacuum-aligned energy level diagram. (b) ZnO thickness-dependent work function and Bader charge trends. (c) Total density of states (DOS) near the Fermi level (E_F). (d) Projected density of states (PDOS) for the composite heterojunction. (e) In-plane electronic conductivities (σ/τ) of the constituent components evaluated within the constant relaxation-time approximation. (f) Gap-aligned σ/τ curves of the composite membranes as a function of ZnO thickness (Table S8).

Table 3
Calculated in-plane electronic conductivity descriptors (σ/τ) at 300 K derived from BoltzTraP2.

System	σ/τ (S m^{-1} s^{-1})	Note
ZnO, 16 L	8.12×10^{8}	Gap artifact, use μ curve
Fe_3O_4	3.11×10^{13}	Component slab
ACNT	7.71×10^{17}	Conductive backbone
Fe_3O_4@ACNT	1.34×10^{14}	Interface

disparity demonstrates that while the Fe_3O_4@ACNT hybrid provides background interactions via electrostatic and π-π stacking forces, the exposed ZnO surfaces act as the primary, high-affinity anchoring sites that capture and immobilize incoming cationic contaminants [104–109].

Taken together, these multi-scale theoretical descriptors provide the quantitative atomic and electronic rationale for the experimental trade-offs that dictate the optimal 1.5:1.5 composition ratio. A ZnO-poor matrix preserves the continuous conductive framework required for photothermal activity but suffers from a depletion of high-affinity anchoring and hydrophilic oxide centers. This deficiency curtails the surface water affinity and local hydration layer formation, which explains the degradation of the long-term oil/water separation flux observed in experiments [110–119].

Conversely, an excessively ZnO-rich composition introduces redundant active sites at the expense of the photothermal matrix. Because ZnO is insulating at E_F and possesses a high phonon-dominated bulk thermal conductivity (44–62 W m^{-1} K^{-1} near room temperature) compared to magnetite, overloading the membrane with ZnO induces rapid bulk heat dissipation rather than localized heat confinement.

Therefore, the theoretical analysis confirms that the experimental 1.5:1.5 ratio represents an optimized compromise, successfully decoupling and maximizing ZnO-mediated surface separation and dye-capture functionalities without disrupting the continuous, Fe_3O_4@ACNT-derived photothermal conduction pathways.

4. Conclusions

In summary, this study demonstrates a sustainable and scalable strategy to fabricate multifunctional membrane platforms by surface-modifying a porous, dual-pore-agent rPET/hC/PVP substrate with a ZnO NR/Fe_3O_4@ACNT (1.5:1.5) active layer. Benefiting from optimized interfacial photon harvesting and localized thermal confinement, the composite membrane achieved a rapid temperature rise to 79.53 °C within 50 *s* under 1500 W m^{-2} solar irradiation, yielding a high ice-thawing volumetric flux of 31.93 L m^{-2} h^{-1} bar^{-1}. Furthermore, the hybrid architecture executed efficient emulsified oil-water separation (99.5%) and selective cationic dye decontamination (exceeding 95%) through the synergistic integration of geometric size exclusion and electrostatic interactions. This versatile platform pairs sustainable polymer recycling with high-performance water purification, establishing a promising paradigm for next generation photothermal remediation technologies.

CRediT authorship contribution statement

Zhuomin Jiang: Writing – review & editing, Methodology, Formal analysis, Conceptualization. **Shuqing Piao:** Writing – review & editing, Writing – original draft, Methodology, Formal analysis, Conceptualization. **Daehong Kim:** Data curation, Formal analysis, Methodology, Software. **Yejin Lee:** Methodology, Data curation. **Chuang Zhu:** Writing – review & editing, Methodology. **Jihoon You:** Data curation, Methodology, Software. **Dongwook Kang:** Formal analysis, Methodology, Software. **Won Bo Lee:** Investigation, Project administration, Validation. **Yuanzhe Piao:** Writing – review & editing, Validation, Resources, Funding acquisition. **Kangwon Lee:** Supervision, Project administration, Funding acquisition.

Declaration of competing interest

The authors declare no conflict of interest.

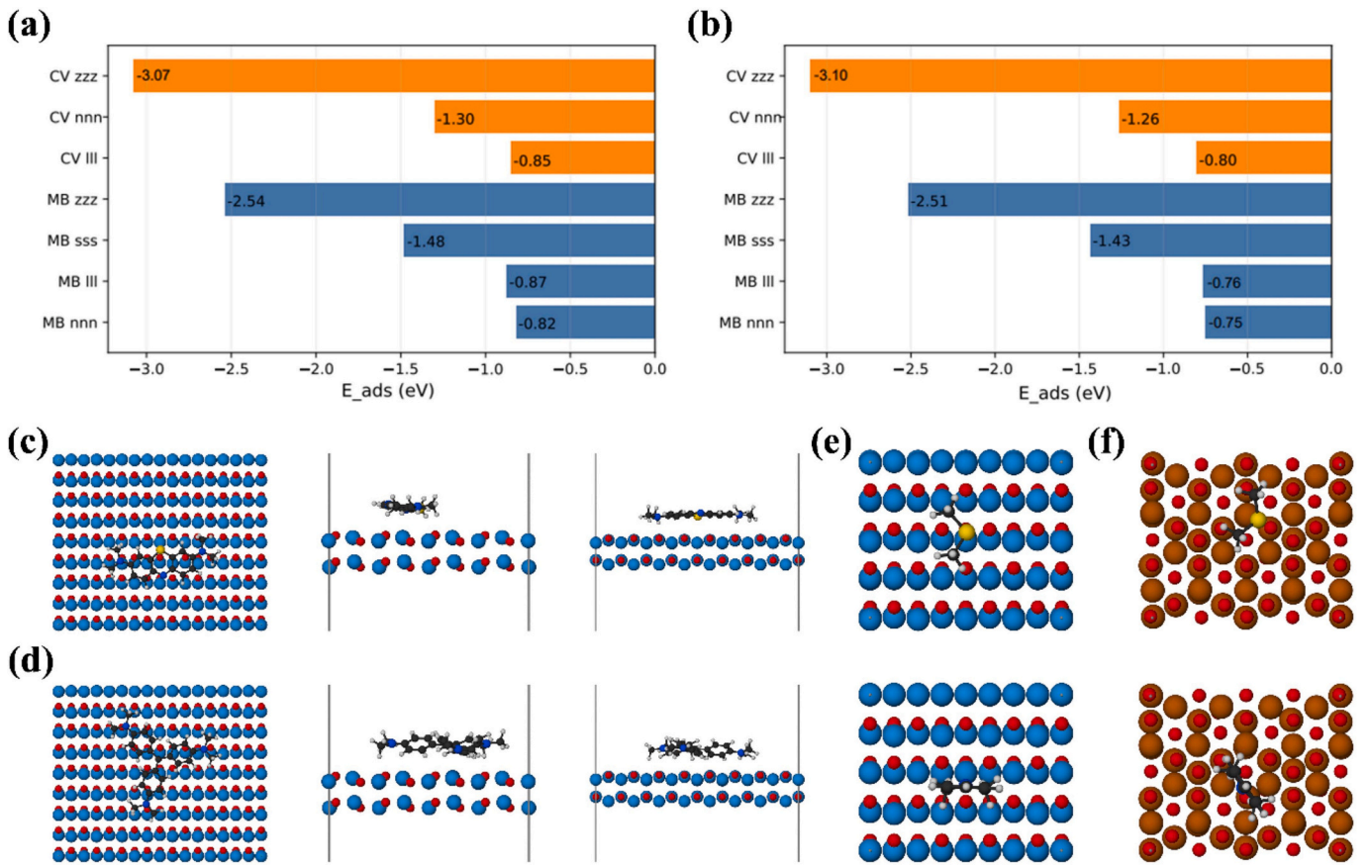

Fig. 8. Geometric orientations, active anchoring fragments, and adsorption thermodynamics of cationic dyes. (a, b) Calculated adsorption energies of full dye molecules evaluated under (a) vacuum and (b) vacuum with dipole corrections. (Table S9-S11 and Fig. S22-S24) (c, d) Three-dimensional views (left to right: top, right, and front views) of the thermodynamically preferred "zzz" orientation for (c) Methylene Blue (MB) and (d) Crystal Violet (CV). (e, f) Optimized adsorption configurations of representative dye fragments (top: dimethyl sulfide, DMS; bottom: *N*,*N*-dimethylaniline, NND) on (e) ZnO and (f) Fe_3O_4 surfaces.

Table 4
Estimated adsorption energies of full dye molecules on the Fe_3O_4 surfaces.

Dye orientation	ZnO neutral vacuum E_{ads} (eV)	Contacts used for the estimate	Fe_3O_4-scale estimate (eV)
MB zzz	−2.54	Two terminal N + central N + central S	~ −0.8
MB sss	−1.48	Central S	~ −1.0
MB lll	−0.87	One terminal N	~ −0.4
MB nnn	−0.82	Central N	~ −0.4
CV zzz	−3.07	Three terminal N	~ −1.8
CV nnn	−1.3	Two terminal N	~ −0.4
CV lll	−0.85	One terminal N	~ −0.4

Note: Values are extrapolated from explicit neutral ZnO adsorption energies based on the energetic offsets derived from the dimethyl sulfide (DMS) and *N*,*N*-dimethylaniline (NND) chemical fragments.

Table 5
Computed binding energies of selective dye chemical motifs.

Surface	Fragment	Interaction motif	Energy (eV)
ZnO	DMS	thiazine-S motif of MB	−2.917
Fe_3O_4	DMS	thiazine-S motif of MB	−2.485
ZnO	NND	tertiary-amine/aromatic motif of MB/CV	−2.018
Fe_3O_4	NND	tertiary-amine/aromatic motif of MB/CV	−1.573

Acknowledgements

This work was in part supported by the Research Institute for Convergence Science, Graduate School of Convergence Science and Technology and Research Institute of Advanced Materials, Seoul National University. This research was supported by Korean Fund for Regenerative Medicine funded by Ministry of Science and ICT, and Ministry of Health and Welfare (25A0207L1), Republic of Korea. This research was also supported by the Higher Education Discipline Innovation Project of China (111 Project, D18012).

Appendix A. Supplementary data

Additional experimental details and supplementary characterization results are provided in the Supporting Information. Supplementary data to this article can be found online at https://doi.org/10.1016/j.cej.2026.180087.

Data availability

Data will be made available on request.

References

[1] M. Sanjrani; A. Nafees; R. Sakina; G. Xue, 2022.
[2] S. Mishra, V. Singh, L. Cheng, A. Hussain, B. Ormeci, J. Environ. Chem. Eng. 10 (2022) 107387.
[3] J. Carrera, T. Vicent, F. Lafuente, Water SA 29 (2003) 11–16.
[4] X. Cui, Q. Ruan, X. Zhuo, X. Xia, J. Hu, R. Fu, Y. Li, J. Wang, H. Xu, Chem. Rev. 123 (2023) 6891–6952.
[5] L.-T. Le, J. Jeon, B.-T. Dang, X.-T. Bui, D. Jahng, Environ. Technol. Innovation 25 (2022) 102178.
[6] Q. Yu, M. Xie, R. Chen, K. Li, L. Zhang, B. Pan, X. Pan, J. Zhang, D. Qu, High-efficiency solar-driven photothermal membrane distillation via permeate-side interfacial heating, Desalination 628 (2026) 120073, https://doi.org/10.1016/j.desal.2026.120073.
[7] Y. Yang, E. Huang, P. Dansawad, Y. Li, Y. Qing, C. Lv, L. Cao, S. You, Y. Li, W. Li, J. Membr. Sci. 687 (2023) 122044.
[8] K. Chaithra, A. Varghese, T. Vinod, S.D. KR, Chem. Eng. J. 499 (2024) 156049.
[9] J.R. Werber, C.O. Osuji, M. Elimelech, Nat. Rev. Mater. 1 (2016) 1–15.
[10] K.J. Howe, M.M. Clark, Environ. Sci. Technol. 36 (2002) 3571–3576.
[11] J. Hoslett, T.M. Massara, S. Malamis, D. Ahmad, I. van den Boogaert, E. Katsou, B. Ahmad, H. Ghazal, S. Simons, L. Wrobel, Sci. Total Environ. 639 (2018) 1268–1282.
[12] C. Kahrs, J. Schwellenbach, Polymer 186 (2020) 122071.
[13] S.A.N. Mehrabani, V. Vatanpour, I. Koyuncu, Sep. Purif. Technol. 298 (2022) 121691.
[14] H.H. Wang, J.T. Jung, J.F. Kim, S. Kim, E. Drioli, Y.M. Lee, J. Membr. Sci. 574 (2019) 44–54.
[15] Y. Hou, P. Shah, V. Constantoudis, E. Gogolides, M. Kappl, H.-J. Butt, Nat. Commun. 14 (2023) 6886.
[16] J. Lin, Z. Yu, T. Chen, J. Huang, L. Chen, J. Li, X. Li, X. Huang, J. Luo, E.Y.M. Ang, Nat. Commun. 16 (2025) 3671.
[17] A. Wang, R. Pan, J. Miao, Y. Lin, Y. Deng, S. Peng, X. Luo, P. Wu, S. Zhang, Y. Wu, Nanomaterials 15 (2025) 1424.
[18] B. Han, J.-C.P. Gabriel, J. Clean. Prod. 480 (2024) 144043.
[19] N. Baig, I. Abdulazeez, N.A. Khan, M.B. Hanif, NPJ Clean Water 7 (2024) 82.
[20] B. Song, Z. Wang, J. Li, M. Luo, P. Cao, C. Zhang, Chem. Eng. J. 426 (2021) 131940.
[21] Y. Zhu, S. Li, Y. Luo, H. Ma, Y. Wang, PeerJ 4 (2016) e2045.
[22] A. Katukiza, M. Ronteltap, C. Niwagaba, F. Kansiime, P. Lens, J. Environ. Manag. 133 (2014) 258–267.
[23] M. Rivero, J. Hu, D. Jaque, M. Canete, J. Sanchez-Marcos, A. Munoz-Bonilla, J. Phys. Chem. C 122 (2018) 16389–16396.
[24] T. Sarkar, S. Tiwari, K. Rawat, P.R. Solanki, H. Bohidar, Colloids Surf. A Physicochem. Eng. Asp. 514 (2017) 218–225.
[25] V. Prasad, C. D'Souza, D. Yadav, A. Shaikh, N. Vigneshwaran, Spectrochim. Acta A Mol. Biomol. Spectrosc. 65 (2006) 173–178.
[26] Y. Wang, H. Liu, Q. Wang, X. An, X. Ji, Z. Tian, S. Liu, G. Yang, Int. J. Biol. Macromol. 253 (2023) 127353.
[27] A. Etale, A.J. Onyianta, J.-C. Eloi, J. Rowlandson, S.J. Eichhorn, Carbohydr. Polym. 325 (2024) 121560.
[28] B. Liu, Y. Li, Y. Yuan, B. Zheng, C. Liu, L. Zhou, J. Zhang, Int. J. Biol. Macromol. 243 (2023) 125119.
[29] E.Y. Astakhov, I. Kolganov, E. Klinshpont, P. Tsarin, A. Kalacheva, Pet. Chem. 52 (2012) 557–564.
[30] J. Zhou, J. Chen, M. He, J. Yao, J. Appl. Polym. Sci. 133 (2016).
[31] T. Istirokhatun, H. Susanto, P. Andarani, A. Filardli, R. Saputra, M. Widada, L. Nurdin, Upcycling of waste PET bottles into functional membranes for water treatment applications, in: IOP Conference Series: Earth and Environmental Science, IOP Publishing, 2025. Vol. 1556. p 012058.
[32] H.T. Nguyen, S.-J. You, Polym. Bull. 82 (2025) 7593–7634.
[33] X. Wang, X.-L. Wang, J. Lv, Z. Wu, J. Zhang, D. Hu, C. Xue, D. Li, X. Zhu, T. Wu, Chem. Eng. J. 422 (2021) 130045.
[34] A. Anjum, R. Garg, M. Kashif, N.O. Eddy, Inorg. Chem. Commun. 178 (2025) 114411.
[35] T. Gogoi, P.G. Ingole, Emerg. Mater. 9 (2026) 46.
[36] R. Edy, X. Huang, Y. Guo, J. Zhang, J. Shi, Nanoscale Res. Lett. 8 (2013) 79.
[37] I. Strain, Q. Wu, A.M. Pourrahimi, M.S. Hedenqvist, R.T. Olsson, R.L. Andersson, J. Mater. Chem. A 3 (2015) 1632–1640.
[38] S. Cichosz, A. Masek, K. Dems-Rudnicka, Sci. Rep. 12 (2022) 19739.
[39] T.K.Q. Doan, K.Y. Chiang, Sustain. Environ. Res. 32 (2022) 26.
[40] W. Wang, Q. Wang, A. Wang, Macromol. Res. 19 (2011) 57–65.
[41] M.D. Nguyen, L. Deng, J.M. Lee, K.M. Resendez, M. Fuller, S. Hoijang, F. Robles-Hernandez, C.W. Chu, D. Litvinov, V.G. Hadjiev, Small 20 (2024) 2402940.
[42] S.S. Wagh, V.S. Kadam, C.V. Jagtap, D.B. Salunkhe, R.S. Patil, H.M. Pathan, S. P. Patole, ACS Omega 8 (2023) 7779–7790.
[43] L. He, X. Liu, C. Han, D. Wang, Q. Wang, X. Deng, C. Zhang, Small Methods 8 (2024) 2301707.
[44] S.K. Mandal, S. Paul, S. Datta, D. Jana, Appl. Surf. Sci. 563 (2021) 150315.
[45] W. Zhang, T. Feng, Y. Wang, X. Dong, D. Wang, F. Wang, D. Ai, H. Li, X. Lv, Q. Ma, R. Guan, C. Zhou, W.W. Yu, Q. Xie, Interfacial functionalization strategies for constructing polymerizable nanomaterials and their polymerized nanohybrid systems, Adv. Colloid Interf. Sci. 354 (2026) 103899, https://doi.org/10.1016/j.cis.2026.103899.
[46] W. Gai, C. Li, Y. Ma, S. Xu, H. Tan, X. Guo, Q. Zhang, C. Liu, K. Zhu, I. Waqar, J. Porous. Mater. 32 (2025) 1279–1291.
[47] R.D. Maalihan, M.R.B. Domalanta, A.C.C. Corrales, E.B. Caldona, Polym. Compos. 46 (2025) 5857–5881.
[48] J. Jordan, K.I. Jacob, R. Tannenbaum, M.A. Sharaf, I. Jasiuk, Mater. Sci. Eng. A 393 (2005) 1–11.
[49] T. Aleem, M. Imran, F. Hussain, A. Asma, A. Arooj, S. Ahmad, A.M. Tighezza, R. Khalil, J. Mol. Graph. Model. 140 (2025) 109118.
[50] T. Tański, M. Zaborowska, W. Matysiak, Arch. Metall. Mater. (2018).
[51] A.M. Vindedahl, J.H. Strehlau, W.A. Arnold, R.L. Penn, Environ. Sci. Nano 3 (2016) 494–505.
[52] J. Song, L. Huang, Y. Lu, X. Liu, X. Deng, X. Yang, S. Huang, J. Sun, Z. Jin, I. P. Parkin, Sci. Rep. 6 (2016) 31818.
[53] L. Liu, X. Li, J. Guo, T. Miao, Z. Ji, X. Wu, C. Chang, J. Membr. Sci. (2025) 124937.
[54] H. Li, S. Gan, C. Yue, Z. Yan, Q. Xue, J. Zhang, T. Yan, H. Zeng, J. Hazard. Mater. 485 (2025) 136397.
[55] M. Gholinia, S. Kiaeian Moosavi, S. Gholinia, D. Ganji, Heat Transfer Asian Res. 48 (2019) 3278–3294.
[56] T. Istirokhatun, S.E. Siahaan, H. Susanto, R.R. Gonzales, A.M.I. Filardli, P. Andarani, H. Matsuyama, J. Clean. Prod. 532 (2025) 146967.
[57] C. Liu, X. Zou, Y. Lv, X. Liu, C. Ma, K. Li, Y. Liu, Y. Chai, L. Liao, J. He, Nat. Nanotechnol. 19 (2024) 448–454.
[58] Y. Zhao, L. Gao, N. Chang, J. Hou, Z. Zhang, Y. Dong, Y. Wang, H. Wang, Sep. Purif. Technol. (2026) 137015.
[59] H.-Z. Gang, M.-N. Yang, Q.-Q. Chen, Z.-Q. Su, G.-Z. Sun, W.-D. Wang, S.-Z. Yang, Y.-C. Li, B.-Z. Mu, Geoenergy Science and Engineering 251 (2025) 213902.
[60] O.T. Mahlangu, M.M. Motsa, H. Richards, B.B. Mamba, M.J. George, L. N. Nthunya, Environ. Nanotechnol. Monit. Manag. 22 (2024) 100984.
[61] S.V. Nipane, P.V. Korake, G. Gokavi, Ceram. Int. 41 (2015) 4549–4557.
[62] A. Stegarescu, H. Cabrera, H. Budasheva, M.-L. Soran, I. Lung, F. Limosani, D. Korte, M. Amati, G. Borodi, I. Kacso, Nanomaterials 12 (2022) 3008.
[63] R. Aviles-Monreal, H. Borbon-Nuñez, K. Fonseca-Flores, M.H. Farías, F. Castillón-Barraza, Nano Express (2025).
[64] A.M. Gheitaghy, A. Ghaderi, S. Vollebregt, M. Ahmadi, R. Wolffenbuttel, G. Q. Zhang, Mater. Res. Bull. 126 (2020) 110821.
[65] L. Wang, C. Wang, W. Zhang, H. Zhu, J. Jin, D. Yin, W. Liao, J. Su, J. Energy Chem. (2025).
[66] J. Wang, Y. Kong, Z. Liu, H. Wang, Solar-driven interfacial evaporation: Design and application progress of structural evaporators and functional distillers, Nano Energy 108 (2023) 108115, https://doi.org/10.1016/j.nanoen.2022.108115.
[67] J. Kim, S. Lee, S.I. Park, J. Baek, D. Seo, G.-M. Choi, J. An, J. Cho, Acta Mater. 277 (2024) 120165.
[68] J. Hao, J. Li, L. Wang, M. He, J. Wang, X. Wang, X. Zhang, J. Xin, J. Membr. Sci. 724 (2025) 123993.
[69] N. Hampu, J.R. Werber, W.Y. Chan, E.C. Feinberg, M.A. Hillmyer, ACS Nano 14 (2020) 16446–16471.
[70] R. Wang, S. Lin, J. Membr. Sci. 620 (2021) 118809.
[71] L. Catala, T. Mallah, Coord. Chem. Rev. 346 (2017) 32–61.
[72] S. Ahmad, M. Imran, F. Hussain, N.A. Niaz, A.M. Tighezza, R. Khalil, M. Irfan, M. F. Ehsan, Surf. Interfaces 54 (2024) 105187.
[73] S. Ahmad, M. Imran, N.A. Niaz, F. Hussain, U. Rasheed, A.M. Tighezza, R. Khalil, M. Irfan, J. Energy Storage 99 (2024) 113206.
[74] V.C. Agulto, I.J. Agulo, R.V. Sarmago, FTIR and UV-visible absorbance studies of hydrothermally grown ZnO coated with polyvinylpyrrolidone, in: Materials Science Forum, Trans Tech Publ, 2017, pp. 73–78. Vol. 895.
[75] X. Lu, M. Niu, R. Qiao, M. Gao, J. Phys. Chem. B 112 (2008) 14390–14394.
[76] A.H. Castro Neto, F. Guinea, N.M. Peres, K.S. Novoselov, A.K. Geim, Rev. Mod. Phys. 81 (2009) 109–162.
[77] A.A. Balandin, S. Ghosh, W. Bao, I. Calizo, D. Teweldebrhan, F. Miao, C.N. Lau, Nano Lett. 8 (2008) 902–907.
[78] S. Li, L. Huang, H. Zhang, Z. Huang, Q. Jia, S. Zhang, Appl. Surf. Sci. 540 (2021) 148386.
[79] S. Ahmad, M. Imran, F. Hussain, U. Rasheed, A.M. Tighezza, R. Khalil, M. N. Ashiq, M. Irfan, M.F. Ehsan, J. Energy Storage 113 (2025) 115728.
[80] M. Shiraishi, M. Ata, Carbon 39 (2001) 1913–1917.
[81] A. Janotti, C.G. Van de Walle, Phys. Rev. B Condens. Matter Mater. Phys. 76 (2007) 165202.
[82] K. Harun, N. Salleh, B. Deghfel, M. Yaakob, A. Mohamad, DFT+ U calculations for electronic, structural, and optical properties of ZnO wurtzite structure: a review, Results Phys. 16 (2020) 102829.
[83] O. Bovgyra; M. Kovalenko; V. Y. Dzikovskyi; A. Vaskiv; M. Y. Sheremeta, 2020.
[84] G.A. Slack, Phys. Rev. 126 (1962) 427.
[85] X. Wu, J. Lee, V. Varshney, J.L. Wohlwend, A.K. Roy, T. Luo, Sci. Rep. 6 (2016) 22504.
[86] M. Sajid, A. Arooj, A. Asma, S. Ahmad, M. Imran, F. Hussain, A.M. Tighezza, R. Khalil, M. Shoaib, J. Phys. Chem. Solids 208 (2026) 112996.
[87] A. Arooj, M. Imran, S. Ahmad, M.K. Gatasheh, F. Hussain, S.M. Ali, R.M.A. Khalil, M.F. Ehsan, J. Phys. Chem. Solids 203 (2025) 112714.
[88] N.-W. Park, W.-Y. Lee, J.-A. Kim, K. Song, H. Lim, W.-D. Kim, S.-G. Yoon, S.-K. Lee, Nanoscale Res. Lett. 9 (2014) 96.
[89] R. Rathnasekara, G. Mayberry, P. Hari, Materials 15 (2022) 8816.
[90] V.P. Zhukov, V.G. Tyuterev, E.V. Chulkov, J. Phys. Condens. Matter 24 (2012) 405802.
[91] A.M. Ganose, J. Park, A. Faghaninia, R. Woods-Robinson, K.A. Persson, A. Jain, Nat. Commun. 12 (2021) 2222.
[92] Y.-K. Kwon, P. Kim, Unusually High Thermal Conductivity in Carbon Nanotubes, in: High Thermal Conductivity Materials, Springer, 2006, pp. 227–265.

[93] S.-Y. Yue, T. Ouyang, M. Hu, Sci. Rep. 5 (2015) 15440.
[94] K. Sääskilahti, J. Oksanen, S. Volz, J. Tulkki, Phys. Rev. B 91 (2015) 115426.
[95] E. Pop, D. Mann, Q. Wang, K. Goodson, H. Dai, Nano Lett. 6 (2006) 96–100.
[96] P. Kim, L. Shi, A. Majumdar, P.L. McEuen, Phys. Rev. Lett. 87 (2001) 215502.
[97] K. Mathew, R. Sundararaman, K. Letchworth-Weaver, T. Arias, R.G. Hennig, J. Chem. Phys. 140 (2014).
[98] K. Mathew, V. Kolluru, S. Mula, S.N. Steinmann, R.G. Hennig, J. Chem. Phys. 151 (2019).
[99] M. Rutter, Electron. Struct. 3 (2021) 015002.
[100] S. Ringe, N.G. Hormann, H. Oberhofer, K. Reuter, Chem. Rev. 122 (2021) 10777–10820.
[101] S. Krukowski, P. Kempisty, P. Strak, Prog. Surf. Sci. 101 (2026) 100809.
[102] N. Bonnet, N. Marzari, J. Phys. Chem. C 129 (2025) 10038–10043.
[103] N. Bano, S.I.A. Shah, A. Sattar, A. Shahsawar, S. Ahmad, F. Hussain, I. Shakir, K. F. Fawy, M.N. Ashiq, Int. J. Hydrog. Energy 204 (2026) 153297.
[104] M. Irani, T. Mohammadi, S. Mohebbi, J. Mex. Chem. Soc. 60 (2016) 218–225.
[105] M.A. Habib, M. Muslim, M.T. Shahadat, M.N. Islam, I.M.I. Ismail, T.S.A. Islam, A. J. Mahmood, J. Nanostructure Chem. 3 (2013) 70.
[106] P. Sun, C. Hui, R. Azim Khan, J. Du, Q. Zhang, Y.-H. Zhao, Sci. Rep. 5 (2015) 12638.
[107] A.S.A. Sharib, A. Bonilla-Petriciolet, A.Q. Selim, E.A. Mohamed, M.K. Seliem, J. Environ. Chem. Eng. 9 (2021) 106220.
[108] W. Jiang, Y. Xia, A. Pan, Y. Luo, Y. Su, S. Zhao, T. Wang, L. Zhao, Chemosensors 10 (2022) 436.
[109] H. Liu, Q. An, Q. Deng, J. Ming, H. Xu, J. Phys. Chem. Solids 174 (2023) 111151.
[110] F.U. Ahmed, D. Upadhaya, D.D. Purkayastha, M.G. Krishna, J. Membr. Sci. 659 (2022) 120803.
[111] F.U. Ahmed, D.D. Purkayastha, J. Environ. Chem. Eng. 11 (2023) 111166.
[112] Z. Liu, B.-B. Wang, Z.-M. Xu, J.-W. Deng, W.-M. Yan, J. Water Process Eng. 56 (2023) 104564.
[113] Z. Liu, P. Wang, J. Jing, M. Li, Y. Fu, X. Zhang, H. Wang, Polymer 325 (2025) 128285.
[114] K. Wang, D.S. Han, W. Yiming, S. Ahzi, A. Abdel-Wahab, Z. Liu, Sci. Rep. 7 (2017) 16081.
[115] Q. You, G. Ran, C. Wang, Y. Zhao, Q. Song, Sep. Purif. Technol. 193 (2018) 21–28.
[116] A. Bajpayee, T.E. Alivio, P. McKay, S. Banerjee, Energy Fuel 33 (2019) 5024–5034.
[117] L. Zhang, L. Li, Z.-M. Dang, J. Colloid Interface Sci. 463 (2016) 266–271.
[118] A.K. El-Sawaf, M. Hemdan, H. Selim, A.A. Nassar, M.F. Mubarak, Surf. Interfaces 46 (2024) 104142.
[119] Z. Zhu, Z. Yu, F.F. Yun, D. Pan, Y. Tian, L. Jiang, X. Wang, Natl. Sci. Rev. 8 (2021) nwaa166.